Technische Universität München
Fakultät für Physik

Bachelor thesis in physics

Electron Identification and Hadron Contamination Studies in Proton-Proton Collisions at $\sqrt{s} = 7$ TeV at the LHC with ALICE

Elektronenidentifikation und Kontaminationsstudien in Proton-Proton Kollisionen bei $\sqrt{s} = 7$ TeV am LHC mit ALICE

Anisa Dashi

Monday, 30^{th} November 2015

Primary reviewer: Prof. Laura Fabbietti
Secondary reviewer: Prof. Peter Fierlinger

Supervisor: Dr. Torsten Dahms

Contents

Abstract v

Kurzdarstellung vi

1 Introduction 1

2 Particle Identification with ALICE 5
2.1 Setup of the ALICE Detector 5
2.1.1 Inner Tracking System 6
2.1.2 Time Projection Chamber 7
2.1.3 Time Of Flight Detector 8
2.1.4 V0 Detector 9
2.2 Particle Identification Methods 9
2.2.1 Track Reconstruction 9
2.2.2 Specific Energy Loss 10
2.2.3 Time of Flight 14

3 Data Analysis 17
3.1 Electron Identification 17
3.1.1 Event and Track Selection 17
3.1.2 PID 18
3.2 Electron Pair Analysis 25
3.2.1 Signal and Background Estimation 25
3.2.2 Signal to Background Ratio and Statistical Significance 28
3.3 Signal Purity Studies 32
3.3.1 TOF-based Approach 32
3.3.2 TPC-based Approach 39

4 Results 45
4.1 Single Electron Purity and Efficiency 45
4.2 Dielectron Purity 48
4.2.1 Signal Purity 49

5 Summary and Outlook 53

A Complete List of the TOF-based Approach 55

B Complete List of the TPC-based Approach 57

Bibliography 61

Acknowledgements 63

Abstract

The continuum of electron-positron pairs, produced in heavy-ion collisions, provides an excellent probe of the quark-gluon plasma and a possible chiral symmetry restoration, since these particles do not undergo strong final state interactions and hence carry information about the in-medium properties of hadrons to the detectors. To extract possible signatures, it is important to work with an electron sample of high purity, i. e. not contaminated by other particles. Dielectrons are also studied in proton-proton collisions to provide a crucial reference for the measurement in heavy-ion collisions.

This thesis presents an analysis performed on a data set of pp collisions at $\sqrt{s}$ = 7 TeV measured with the ALICE detector at the Large Hadron Collider. The aim of this work is to optimize the electron identification and to reduce the hadron contamination. For that, four different combinations of particle identification (PID) criteria are compared regarding the statistical significance S/σ_S of their dielectron signals and their electron purities. The analysis shows that one can achieve good electron identification efficiencies and high electron purities by combining the specific energy loss signals measured in the Inner Tracking System and the Time Projection Chamber with the information of the Time of Flight detector. With such a PID selection one obtains a dielectron signal with a purity higher than 82% reaching up to 96%, depending on the invariant mass.

Kurzdarstellung

Das Kontinuum von Elektron-Positron Paaren, produziert in Schwerionenkollisionen, enthält wichtige Informationen über das Quark-Gluon Plasma und die mögliche Wiederherstellung der chiralen Symmetrie, da diese Teilchen nicht über die starke Kernkraft wechselwirken und daher Informationen über die Eigenschaften der Hadronen im Medium enthalten. Um mögliche Signaturen dafür zu extrahieren, ist es wichtig, Elektronen mit hoher Reinheit zu identifizieren, d. h. das möglichst wenige andere Teilchen als Elektronen fehlidentifiziert werden. Dielektronen werden auch in Proton-Proton Kollisionen gemessen, um eine unverzichtbare Referenz für die Messung in Schwerionenkollisionen zu dienen.

Diese Arbeit stellt eine Analyse vor, die einen Datensatz von pp Kollisionen bei $\sqrt{s}$ = 7 TeV untersucht, der mit dem ALICE Detektor am Large Hadron Collider aufgezeichnet wurde. Das Ziel dieser Arbeit ist die Optimierung der Elektronenidentifikation und die Reduzierung der Hadronenkontamination. Hierzu werden vier verschiedene Kombinationen von Detektorsignalen zur Teilchenidentifizierung bezüglich der statistischen Signifikanz S/σ_S ihrer Dielektronen-Signale und der Reinheit der Elektronenkandidaten verglichen. Die Analyse zeigt, dass man gute Elektronenidentifikationseffizienzen sowie eine hohe Reinheit der Elektronenkandidaten erreichen kann, indem man die spezifischen Energieverlust-Signale des inneren Silizium-Halbleiterdetektors und der Zeitprojektionskammer mit Informationen des Flugzeitdetektors kombiniert. Das Signal, das man mit solch einer Elektronenidentifizierung erhält, besitzt eine Reinheit von mehr als 82%, die in Abhängigkeit von der Dielektronenmasse bis auf 96% ansteigt.

Chapter 1

Introduction

Dileptons, i.e. electron-positron or muon pairs, are one of the most useful probes to study the quark-gluon plasma (QGP) and chiral symmetry restoration (CSR). The QGP is an extreme state of matter where quarks and gluons are deconfined. Under normal conditions, hadronic matter consists of confined quarks that interact via the exchange of gluons, the carriers of the color-charge in the strong interaction, as described by the theory of quantum chromodynamics (QCD). The quarks are bound into color-neutral baryons (three quarks) and mesons (one quark and one antiquark) and cannot be observed as single particles with a determined color charge. However, at high energy densities of 1 GeV/fm^3 [1] and high temperatures of $\approx$ 160 MeV a new medium is created, the QGP, where quarks and gluons are deconfined, i.e. no longer bound to hadrons. The QGP as a whole must still be color-neutral. This state of matter is of great interest to physics since it may have existed in the early universe, a few microseconds after the big-bang, and could still exist in the core of very dense neutron stars. The only way to investigate QGP experimentally is to create it in the laboratory. For that, heavy ions, like gold or lead nuclei, are collided at very high energies. Such experiments are carried out at the Relativistic Heavy Ion Collider (RHIC) at the Brookhaven National Laboratory in the USA and at the Large Hadron Collider (LHC) at CERN in Switzerland. The latter reached in 2015 center of mass energies $\sqrt{s}$ = 13 TeV in proton-proton collisions and 5.02 TeV per nucleon-nucleon pair in lead-lead collisions, which are the highest energies reached so far in a collider experiment. In a lead-lead collision, the nucleon-nucleon interactions produce many particles which constitute a hot and dense matter where the quarks undergo deconfinement. The medium expands and the energy density decreases, so that hadronization occurs, i.e. the quarks are confined in hadrons again. Properties of the QGP can then be derived from the particles created in the collision.

Furthermore, investigating nuclear matter under extreme conditions can improve our understanding of quantum chromodynamics since chiral symmetry is predicted to be restored along with the transition to the deconfined phase. Chirality is a property of particles which distinguishes between left-handed and right-handed particles. If the chiral symmetry is conserved, left- and right-handed particles do not mix with each other. This would be the case if quarks had zero mass, but the non-vanishing

quark masses lead to a mass term in the QCD Lagrangian that breaks the chiral symmetry explicitly. However, this term is not sufficient to explain the big mass difference between chiral partners, like the a_1 and ρ mesons (Δm = 500 MeV). Besides the explicit symmetry breaking in fact, chiral symmetry is also spontaneously broken due to the vacuum expectation value of the quark condensate, $\langle \bar{q}q \rangle$, being not equal to zero. If chiral symmetry is conserved, the potential of the system is symmetric with a symmetric ground state, where deviations in any direction do not cost energy and hence produce massless particles. In the case of a spontaneously broken symmetry, the previous potential minimum becomes a local maximum and the system is described by a symmetric potential with an infinite number of degenerate ground states. The random choice of one of them breaks the symmetry of the system and small deviations in direction of the local maximum cost energy, hence producing massive particles. Numerical QCD calculations show that at high temperature and/or high baryon density deconfinement of quarks and gluons takes place. This leads to a vacuum expectation value $\langle \bar{q}q \rangle \approx 0$ and a symmetric ground state of the potential, i.e. chiral symmetry is restored. Furthermore, lattice QCD calculations predict a partial CSR to occur already before deconfinement, as can be seen in figure 1.1, which shows the order parameters of deconfinement (on the left) and of chiral symmetry (on the right) as a function of temperature [2]. The deconfinement order parameter approaches 1 for high temperatures, while the chiral symmetry order parameter goes to zero. Already below the predicted phase transition temperature of 160 MeV, chiral symmetry is largely restored. This restoration affects the hadron spectral properties, i.e. mass m and width Γ. For example, the spectral functions of the a_1 and ρ mesons must have the same shape after CSR. It is unclear how this is realized in nature but two different predictions exist: the Brown-Rho scaling, where both particle masses become smaller than in the broken symmetry, and broadening, where the widths get larger. This was already investigated by experiments at the SPS (Super Proton Synchrotron) and RHIC, and the data seem to prefer the broadening hypothesis [3–8].

To investigate CSR after the collision, a probe is needed that carries information about hadron spectral properties to the detectors, i.e. it must be related to the hadrons in medium and must leave the collision system without undergoing strong final state interactions. The perfect and only known probe is found in dileptons coming from vector meson decays, like ρ, ω and ϕ, since their invariant masses m_{ee} correspond to the masses of the vector mesons at the time of the decay and, as they undergo only electromagnetic interactions, they do not strongly interact with the hadronic medium after being emitted. The most appropriate is the ρ meson since it decays in the medium due to its short life time (τ = 1.3 fm/c) in comparison to the life time of the medium, which is $\approx$ 10 fm/c. With τ = 23 and 44 fm/c respectively, the ω and ϕ mesons decay mostly after the hadronization process, i.e. the dileptons do not carry information about their in-medium properties. The chiral partner of

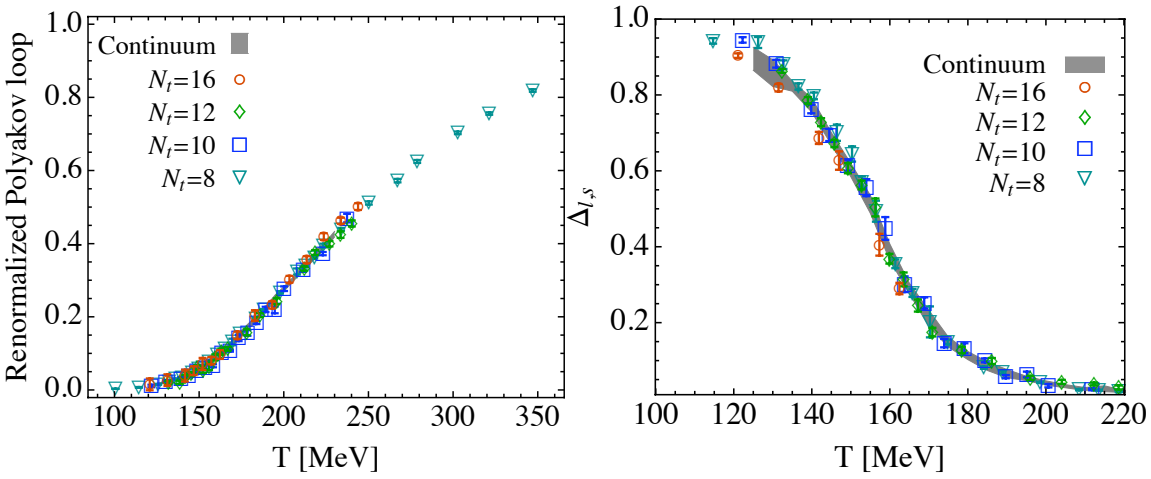

(a) deconfinement order parameter

(b) chiral symmetry order parameter

Figure 1.1: Order parameters of deconfinement (left) and of chiral symmetry (right) as a function of temperature [2]. Chiral symmetry is predicted to be largely restored already at T = 160 MeV, while quarks and gluons are still subject to confinement effects.

the ρ meson, the a_1, is not appropriate to study CSR since it decays in three pions, which can strongly interact with the medium after emission.

Dileptons are produced by different processes at all stages of the collision, hence their invariant mass spectrum contains various contributions. From this spectrum not only information about CSR can be gained, but also effects of the QGP on heavy quarks can be studied from modifications of the intermediate mass region, i.e. $1.2 < m_{ee} < 2.9$ GeV/c. Dileptons are also a useful tool to determine the temperature of the produced medium by measuring the energy spectrum of thermal radiation, i.e. virtual photons with a non-zero mass, γ^*, which can convert to electron-positron pairs.

To extract possible hints for chiral symmetry restoration or QGP from the continuum of e^+e^- pairs, it is essential to work with a high purity sample of electrons and positrons, i.e. that is not contaminated by hadrons. Besides in heavy-ion collisions, it is important to study dielectrons also in proton-proton collisions, where QGP and CSR are not expected due to the insufficient energy density, in order to have reference data which are crucial for the interpretation of the heavy-ion data. In this thesis, a data set of 200 million proton-proton collisions at $\sqrt{s} = 7$ TeV measured with ALICE (A Large Ion Collider Experiment) at the LHC in 2010 is analyzed with the aim of obtaining a high purity electron sample. The ALICE detector is described

in the next Chapter, followed by a detailed analysis description in Chapter 3. Results and summary of the analysis are discussed in Chapter 4 and 5, respectively.

Chapter 2

Particle Identification with ALICE

2.1 Setup of the ALICE Detector

The ALICE apparatus, shown in figure 2.1, comprises seventeen detector subsystems divided into three categories: central-barrel detectors, forward detectors and the muon spectrometer. The central-barrel detectors are used to reconstruct charged particles and photons. The reconstruction of charged particles is possible for $p_T > 0.15$ GeV/c in the pseudorapidity range $|\eta| < 0.9$ over the full azimuthal angle. Transverse momentum, p_T, is the projection of the momentum vector onto the transverse plane, perpendicular to the z-axis, which is defined as the beam direction, while pseudorapidity, η, is defined as follows:

$$\eta = -\ln\left(\tan\frac{\theta}{2}\right) \tag{2.1}$$

with θ being the polar angle, i.e. polar angles from 45° to 135° are covered. The central-barrel detectors are enclosed in a solenoid magnet with a magnetic field of 0.5 T parallel to the z-axis that allows the p_T determination of charged particles. These are the Inner Tracking System (ITS), Time Projection Chamber (TPC), Transition Radiation Detector (TRD), Time Of Flight (TOF), two electromagnetic Calorimeters (PHOS and EMCal) and a ring imaging Cherenkov detector (HMPID - High Momentum Particle Identification Detector) [10]. These subsystems are used to identify charged particles up to 20 GeV/c [10].

The forward detectors, like V0 and ZDC (Zero Degree Calorimeter), are located at small polar angles and used for global event characterization and triggering [11]. A trigger decision is used to select events for readout.

This analysis makes use of the ITS, TPC and TOF detectors, which are described in the next sections. The V0 detector is shortly described as well because it served as minimum bias (MB) trigger to record the data set used for this work. Although the TRD is specialized in the identification of electrons, it will not be used here for two reasons: first, in 2010 only seven of the 18 super-modules of the TRD were installed, which leads to a limited acceptance of the detector, and second, it identifies electrons only for $p_T > 1$ GeV/c [10], while this analysis focuses on the electron identification

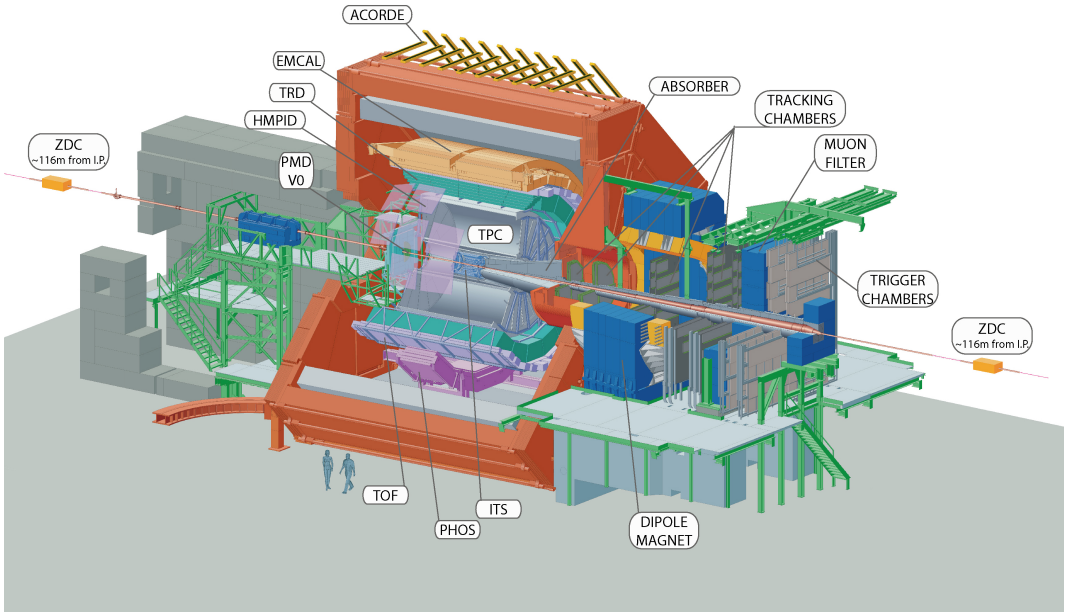

Figure 2.1: Setup of the ALICE detector system [9].

at lower momenta. The usage of the TRD is foreseen in the analysis of new data from the second period of LHC operation (2015–2018), for which all the TRD modules were installed and included into data taking.

2.1.1 Inner Tracking System

The Inner Tracking System (ITS) is the first detector surrounding the beam pipe. The ITS is used for primary vertex determination, secondary vertices reconstruction and particle identification at low transverse momenta. The primary vertex is defined as the collision point while a secondary vertex is the decay point of a long-lived, i.e. weakly decaying, particle. Other important tasks of the ITS are to reconstruct tracks of particles going through dead zones of the TPC (due to the azimuthal segmentation) and to improve momentum and angular resolution for particles reconstructed in the TPC [11].

Six cylindrical silicon layers compose the ITS, as shown in figure 2.2. The innermost two layers are Silicon Pixel Detectors (SPD), the following two are Silicon Drift Detectors (SDD) and the two outer layers are Silicon micro-Strip Detectors (SSD). The SPD has to cope with very high track densities (up to ~ 50 particles per cm^2 in Pb-Pb collisions) and is a crucial element of the primary vertex determination. The

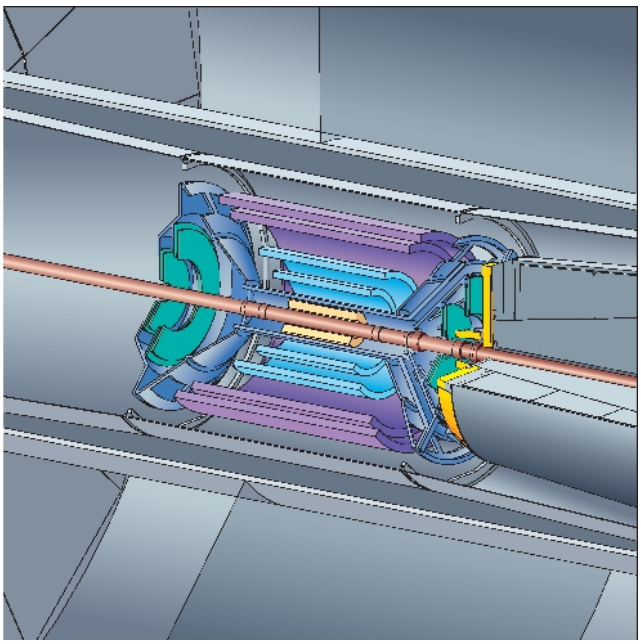

Figure 2.2: The ITS detector [9].

SSD matches the tracks from the TPC to the ITS measuring the track position in two dimensions (ϕ and z). Together with the two middle layers it also contributes to the particle identification providing energy loss information, thanks to the analog signal readout [11].

2.1.2 Time Projection Chamber

The Time Projection Chamber (TPC) surrounds the ITS and is the main component of the ALICE detector. A schematic view can be seen in figure 2.3. Its main tasks are to measure charged particle momenta with good two-track separation and to identify particles via their specific energy loss [11]. The TPC is made of a cylindrical field cage, separated in two parts by a high voltage electrode at the center, and multi-wire proportional chambers with cathode pad readout at each endplate. Between the endplates and the central electrode a voltage of 100 kV is applied to create a uniform electric field along the cylinder axis, which is aligned with the beam direction. The field cage is filled with a $Ne/CO_2/N_2$ (90/10/5) gas mixture, optimized to reduce multiple scattering. Transverse momenta of charged particles can be measured over a large interval, from 0.1 GeV/c up to 100 GeV/c [11].

The TPC is a gaseous ionization detector, i.e. the charged particles created in a collision ionize the TPC gas, producing free electrons. These electrons drift towards

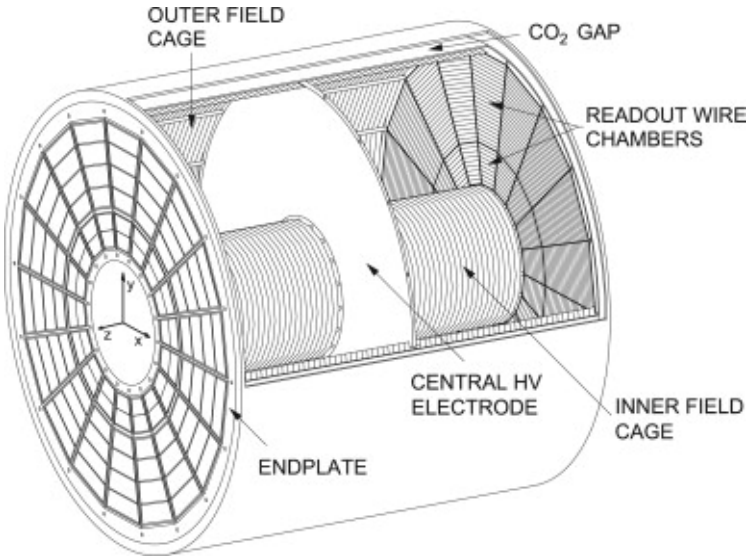

Figure 2.3: Setup of the TPC detector [12].

the endcaps under the influence of the electric field and reach the readout chambers, where their position and arrival time are accurately measured [12]. The position measurement allows the reconstruction of a two dimensional projection in the transverse plane (x,y) of the trajectory of the ionizing particles. The third dimension is reconstructed from the time of arrival at the endplates (relative to some external reference such as the collision time of the beams from the LHC [12]), since the drift velocity of the electrons from ionization, given by

$$v = \frac{eE\tau}{m_e}, \tag{2.2}$$

is approximately constant while traversing the gas (with τ the mean collision time, E the electric field, e the elementary charge and m_e the electron mass) [13]. Therefore, from the drift time one can calculate the production point along the beam axis [14]. In this way the complete trajectory in space is precisely determined for all charged particles.

2.1.3 Time Of Flight Detector

The Time-Of-Flight (TOF) detector is a cylindrical shell consisting of an array of Multi-gap Resistive Plate Chambers (MRPCs) with a modular structure and a high and uniform electric field over the full volume of the detector, which is filled with a gas mixture containing carbon, fluorine and sulfur [11]. It can improve track reconstruction when coupled with the ITS and TPC detectors. The main function

of the TOF is to help with the particle identification in the low and intermediate momentum range (pion and kaon identification up to 2.5 GeV/c and proton identification up to 4 GeV/c) [15]. This is possible thanks to the information that this detector provides about the time of flight t_{TOF} of the particles since, from the known momentum p and track length l, this can be related to the particle velocity

$$\beta = \frac{l}{t_{TOF}c} \tag{2.3}$$

and mass [16]

$$m = \frac{p}{\beta\gamma} = \frac{p}{c}\sqrt{\frac{c^2 t_{TOF}^2}{l^2} - 1}. \tag{2.4}$$

2.1.4 V0 Detector

The V0 detector consists of two arrays of scintillators, the V0A and the V0C: the first one is located 340 cm from the interaction point on the opposite side to the muon spectrometer and covers the pseudorapidity range $2.8 < |\eta| < 5.1$, the second one covers the range $-3.7 < |\eta| < -1.7$ and is fixed on the front face of the hadronic absorber of the muon spectrometer (see figure 2.1) [11]. The V0 system is mainly used for trigger definition, like the minimum bias trigger. For the 2010 pp data the MB trigger required a coincidence signal on both sides of V0 (that indicates a beam-beam interaction), a hit in the SPD layers of the ITS detector (a hint for activity in the central pseudorapidity region, i.e. an inelastic pp collision) and the rejection of interactions between the beam and the residual gas in the beam pipe. Besides the trigger function other important tasks of the V0 detector are to measure luminosity, particle multiplicity and centrality of the collision (i.e. the initial overlap region of the colliding nuclei in heavy-ion collisions), as well as to monitor LHC beam conditions [17].

2.2 Particle Identification Methods

2.2.1 Track Reconstruction

The method used for track finding and fitting in the central barrel is the Kalman filter algorithm [11]. The track reconstruction consists of four steps: finding tracks in the TPC, propagating them to the ITS, following the tracks again outwards and prolonging them inwards again in the final stage of the reconstruction.

In the first step, the seeding for the Kalman filter is done, i.e. a set of initial seed values for the track parameters is determined for each track candidate. To do that, one uses the space points reconstructed in the TPC and starts combining the points from the outermost pad rows, following then the track towards the center of the

TPC. For each pad row where a space point compatible with the track prolongation is found, the track parameters are updated, taking into account energy loss and multiple scattering. This procedure is done twice, first assuming that the track originated from the primary vertex and then assuming that it comes from a secondary vertex.

In the second step, the tracks reconstructed in the TPC are propagated in the outer layers of the ITS. The track parameters are updated when a space point is found within the search window around the track prolongation. If several space point candidates are found, each of them is followed independently from the others towards the innermost layers of the ITS. In this way, every TPC track has more than one path candidate in the ITS and the right one is chosen only at the end on the basis of a χ^2 minimization method.

In the third step, the track is followed from the innermost ITS layers outwards. Since the track parameters are much more precise than in the first step, it allows discarding points incorrectly assigned before. In this step, the tracks are followed also beyond the TPC: they are matched with hits in the TOF and associated with space points in the TRD, HMPID and PHOS.

For the last step, the Kalman filter is reversed again and the tracks are refitted from the outside inwards. With this step, the final values of the track parameters are obtained.

To find tracks of particles that go through dead zones of the TPC, i.e. for which no seeding for the Kalman filter is possible, an additional step can be done considering only the space points that remain in the ITS after removing the points already assigned to tracks [11].

After track reconstruction, one of the track parameters, the bending radius r, can be used to determine the transverse momentum of charged particles, which is independent of the particle mass:

$$p_T = 0.3 \frac{\text{GeV}}{\text{Tm}} \cdot qrB, \tag{2.5}$$

where q is the particle charge and B the magnetic field.

2.2.2 Specific Energy Loss

The TPC detector and the four outer layers of the ITS (SDD and SSD) provide information for particle identification (PID) by measuring the mean energy loss of the particles per unit path length $\langle dE/dx \rangle$. The energy loss of charged particles when traversing material is due to the Coulomb interaction with the electrons bound in the atoms of the matter. These interactions ionize the gas in the TPC and excite the electrons from the valence band to the conduction band in the ITS layers,

respectively. Typical values needed for the creation of one electron/ion or one electron/hole pair are around 30 eV for gases and 3.6 eV for silicon (which corresponds approximately to the band gap energy) [16].

The mean energy loss of relativistic particles traversing matter is given by the Bethe-Bloch equation [13], which describes the average dE/dx as a function of the particle velocity $\beta = v/c$:

$$\left\langle -\frac{dE}{dx} \right\rangle = Kz^2 \frac{Z}{A} \frac{1}{\beta^2} \left[\frac{1}{2} \ln \left(\frac{2m_e c^2 \beta^2 \gamma^2 T_{max}}{I^2} \right) - \beta^2 - \frac{\delta(\beta\gamma)}{2} \right]. \tag{2.6}$$

Here are $\gamma = 1/\sqrt{1-\beta^2}$, Z and A the atomic number and atomic mass of the absorber, z the atomic number of the incident particle, T_{max} the maximum kinetic energy that can be transferred to a free electron in a single collision, I the mean excitation energy in eV, $\delta(\beta\gamma)$ the density effect correction and $K = 4\pi N_A r_e^2 m_e c^2$ (N_A is the Avogadro's number). An example of the Bethe-Bloch function for positive muons in copper is shown in figure 2.4. For low energies, $\langle -dE/dx \rangle$ is proportional to $1/\beta^2$. The minimum of the energy loss lies at $\beta\gamma = p/Mc \approx 3$. This is a broad minimum called MIP (Minimum Ionizing Particles) region. For higher energies, in the relativistic rise region, the energy loss increases like $\ln(\beta\gamma)$ approaching the Fermi plateau region for higher velocities. If the measured dE/dx function is combined with the momentum, the mass of the particles can be easily derived, i.e. particles with different masses can be distinguished from each other, as it can be seen in figure 2.5.

In the TPC, the energy loss of a traversing particle is measured by clusters, a combination of hits in the readout pads which are assumed to have been generated from the same ionizing particle. This means they correspond to the energy loss per track length [14]. The total energy loss is the sum of several single scattering processes and therefore undergoes statistical fluctuations due to the number of these processes and to the details of every individual collision. Hence the total energy loss, and with it the signal of the clusters, follows a Landau distribution, which has a long tail at higher energies that comes from rare large energy transfers in a single scattering. Because of this tail, the mean energy loss and the most probable loss do not coincide.

The Landau distribution can be approximated by a Gaussian distribution using the method of the truncated mean, which consists of discarding some of the scattering processes with very high energy loss. In the TPC, this is done removing 40% of the clusters with the highest signal from the calculation of the sum, while in the ITS only the two or three lowest out of four signals provided from the SDD and SSD layers are used [11]. In figure 2.5, the dE/dx distribution of the TPC is shown as a function of momentum. The black lines correspond to the expected value for the energy loss of one particle according to the Bethe-Bloch formula (2.6). The spreading is due to the limited resolution of the detectors ($\approx 5.5\%$ for pp collisions in the TPC and

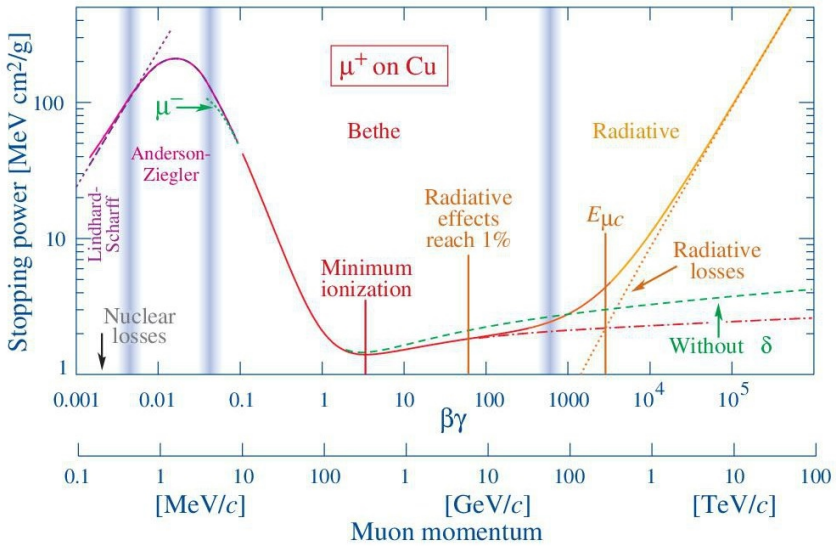

Figure 2.4: Stopping power ($-\langle dE/dx\rangle$) for positive muons in copper as a function of $\beta\gamma$ [13].

$\approx 11\%$ in the ITS). With this method, particles can be identified very well, except for momentum regions where the dE/dx curves overlap and for higher momenta where the bands merge because of the Fermi plateau.

Projecting the dE/dx distribution for a given momentum range, one gets a roughly Gaussian curve for each particle type: e, π, K, p, d. Using the mean and the width (σ) of a Gaussian fit, the dE/dx spectra can be parametrized around the mean energy loss value expected for each particle type. For that the mean energy loss is subtracted from the measured dE/dx value and then the result is divided by the width of the fit:

$$n\sigma_i^{\mathrm{TPC}} = \frac{dE/dx - \langle dE/dx\rangle_i}{\sigma_{dE/dx,i}} \tag{2.7}$$

The energy loss is than expressed in number of sigmas for each particle, with the considered particle type centered at zero. Figure 2.6 shows the $n\sigma_e$ distribution as a function of momentum in the TPC.

From the Gaussian fits of the energy loss distributions one can also get the separation power between two particle types A and B [18]:

$$N\sigma_{A,B}^{\mathrm{TPC}} = \frac{\langle dE/dx\rangle_A - \langle dE/dx\rangle_B}{(\sigma_A + \sigma_B)/2} \tag{2.8}$$

with σ_A and σ_B being the widths of the Gaussian fits for the two particles A and B.

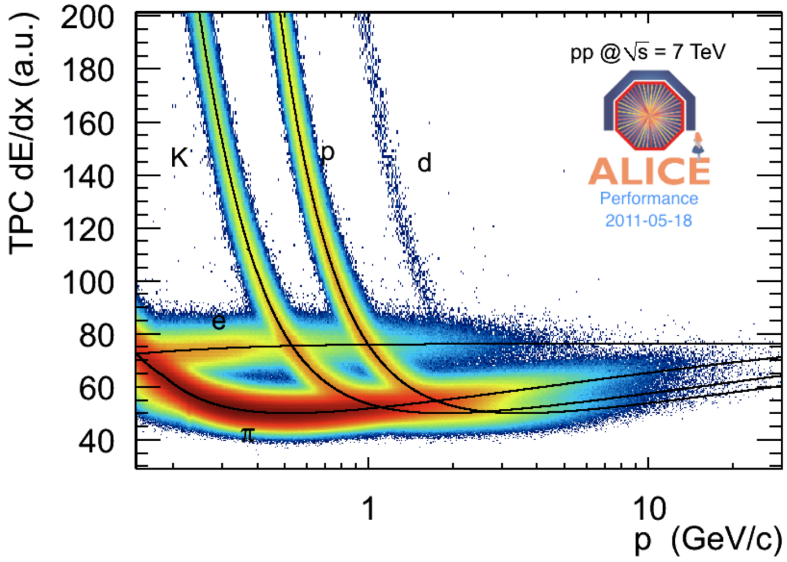

Figure 2.5: The energy loss spectrum of charged particles as a function of momentum measured with the TPC in p+p collisions at $\sqrt{s}$ = 7 TeV [9].

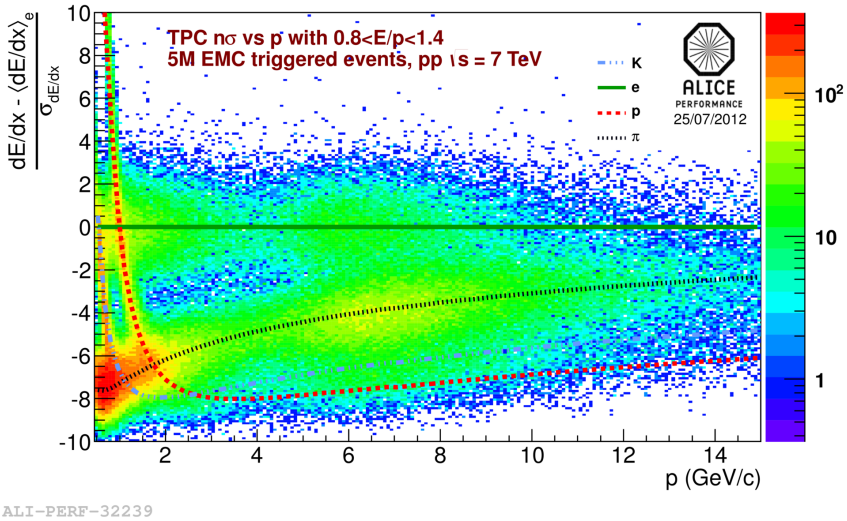

Figure 2.6: The dE/dx distribution parametrized around the expected electron signal as a function of momentum measured in p+p collisions at $\sqrt{s}$ = 7 TeV [9]

For example, the separation power between electrons and pions in the TPC in the momentum range $0.2 < p < 2$ GeV/c is $\gtrsim 6\sigma$.

The ITS energy loss distribution is parametrized in the same way and is expressed in $n\sigma_i^{\mathrm{ITS}}$ for each particle type.

2.2.3 Time of Flight

Measuring the time of flight of charged particles, the TOF detector provides additional information that can be used for PID in the momentum ranges where the TPC energy loss curves of different particles cross each other. The start time for a TOF measurement is given by the T0 detector, which consists of two Cherenkov counters, T0A and T0B, placed in two opposite sides of the interaction point covering, respectively, the pseudorapidity regions $-3.28 < \eta < -2.97$ and $4.61 < \eta < 4.92$ [10]. The average time measured by the two T0 sub-detectors is used as start time: $t_0 = (t_{\mathrm{A}} + t_{\mathrm{B}})/2$.

For the measured time of flight, a Gaussian is considered as response function of the detector [18]:

$$g_i(t_{\mathrm{TOF}}) \approx \frac{1}{\sigma} \exp\left[-\frac{(t_{\mathrm{TOF}} - t_i^{\mathrm{exp}})^2}{2\sigma^2}\right] \tag{2.9}$$

with t_{TOF} the time of flight measured from the TOF detector, t_i^{exp} the expected time of flight for each particle type and $\sigma = \sqrt{\sigma_{\mathrm{TOF}}^2 + \sigma_{\mathrm{rec}}^2}$ the total time of flight resolution, composed of the resolution of the TOF measurement (σ_{TOF}, which also includes the uncertainty on the start time of the measurement) and the uncertainty on the reconstruction of momentum and track length (σ_{rec}) [18].

From the measured time of flight and the reconstructed track length, the velocity spectrum of charged particles as a function of the rigidity p/z (with the charge z) can be determined, as shown in figure 2.7. Every band corresponds to one particle type (positively charged particles on the right side and negatively charged on the left side), while the data outside the bands are due to fake matches of tracks from the TPC to the TOF signal. For momenta lower than 0.3 GeV/c the particles cannot reach the detector since their tracks are bent too much by the magnetic field, hence no TOF signal is available. As it can be seen, the TOF information provides good PID in the momentum range lower than 4 GeV/c, while for bigger momenta the bands merge with each other. This can be easily understood looking at the separation power for two particles A and B with the same momentum but different masses [16]:

$$N\sigma_{\mathrm{A,B}}^{\mathrm{TOF}} = \frac{|t_A - t_B|}{\sigma_{\mathrm{TOF}}} = \frac{Lc}{2p^2\sigma_{\mathrm{TOF}}} \left|m_A^2 - m_B^2\right|. \tag{2.10}$$

Hence two particle types cannot be easily distinguished from each other if their mass difference becomes small compared to their momenta.

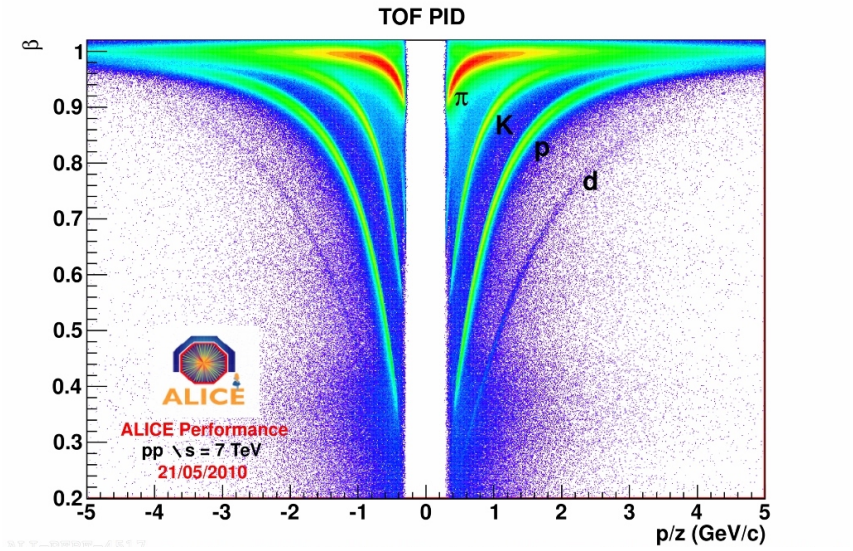

Figure 2.7: Velocity β of charged particles as a function of momentum over charge measured with the TOF detector in p+p collisions at $\sqrt{s} = 7$ TeV [9].

The TOF signal in a given momentum range can be parametrized around the expected velocity value for each particle type, similar as done for the energy loss spectra in the TPC and ITS detectors, i.e. the signal is fitted with a Gaussian. After parametrization a $n\sigma$-distribution as a function of momentum is obtained for each particle type, with $n\sigma$ defined as:

$$n\sigma_i^{\mathrm{TOF}} = \frac{\beta_i - \beta_i^{\mathrm{exp}}}{\sigma_i}. \tag{2.11}$$

Chapter 3

Data Analysis

In this chapter, the analysis is described in detail. It is performed on a data set of pp collisions at $\sqrt{s}$ = 7 TeV with the primary goal of optimizing the electron identification and reducing the hadron contamination. First, several event and track selection criteria are applied to assure a good track quality and then different PID sets are used to identify electrons. After that, the e^+e^- pair analysis is performed and the hadron contamination is measured.

In this analysis, 'electrons' means electrons and positrons together if not stated explicitly. Furthermore, the analysis is performed charge integrated as both electrons and hadron background are produced charge-symmetric at LHC energies.

3.1 Electron Identification

3.1.1 Event and Track Selection

Besides requiring the minimum bias trigger, other event selection criteria are applied in order to reject background events such as beam-gas interactions and cosmic rays. The most important one is a vertex requirement: only events with reconstructed vertex and at least one track contributing to the vertex determination are used for the analysis. Then, the vertex is required to be within 10 cm in z direction from the geometrical center of the ALICE central barrel detectors. The main limitation here is given by the ITS coverage, since the SPD layers are 28 cm long (±14 cm from the center), i.e. for vertices outside this range no hit on the SPD is available, which however is needed for the MB trigger and to assure a good track quality. This vertex selection is also needed to have a uniform acceptance in the TPC for tracks with $|\eta| < 0.8$.

From these events, only tracks that originate from a particle with $p_T > 0.2$ GeV/c and that have been reconstructed in the pseudorapidity range $|\eta| < 0.8$ are accepted. These limits are given from the detector acceptance of the central barrel detectors. Other important selection criteria are applied in order to select only primary particles, i.e. particles that are produced in the initial pp collision or from electromagnetic decays. For that, the distance of closest approach of the track to the vertex

is required to be less than 3 cm in z direction and less than 1 cm in the xy plane. Furthermore, secondary particles that originate from weak decays are rejected using the kink topology: if the track has a kink at some point, it means that the primary particle decayed but one of the produced particles has not been reconstructed and only the track of the other one can be seen, which moves in another direction with respect to the primary particle. The track of this particle is then rejected.

Some other criteria are required for the track reconstruction in the ITS and TPC detectors. For the ITS, the particle must have left a hit in the first SPD layer. This requirement removes external conversions of photons beyond the beam pipe, since a photon converting in the detector material leaves no trace in the first SPD layer. Furthermore, this improves the track parameters near the vertex. Then, for the track reconstruction in the ITS, at least four clusters must have been used. With this cut, it is assured that at least two clusters carry dE/dx information.

In the TPC, at least 80 out of a maximum of 159 available clusters and at least 100 crossed rows are required to have been used for track reconstruction. The number of crossed rows is equal to the number of clusters plus the number of missing clusters used to reconstruct the track, with a missing cluster being assigned to the track if a cluster is found on one of the two neighboring pad rows. Finally, the χ^2 per number of clusters of the track in the TPC is required to be lower than 4, since a large χ^2 means that the track reconstruction is not unequivocal, or that two tracks very close to each other were reconstructed as one.

3.1.2 PID

For the electron identification, the $n\sigma_e$ distributions of particles detected in the ITS, TPC and TOF, that survived the track cuts explained in the previous section, are considered as a function of momentum. As these spectra, shown for example for the TPC in figure 2.6, contain not only electrons, but also pions, kaons, protons and deuterons, a certain $n\sigma_e$ range has to be selected in order to identify electrons and remove hadrons.

The biggest contamination in the electron sample comes from pions, since they are the particles most copiously produced in a collision, being the lightest hadrons. Their production rate is also much larger than the electron one, as pions are produced via strong interactions. Since the TPC has a good electron/pion separation, a first attempt to identify electrons is to select them via the $n\sigma_e^{\mathrm{TPC}}$ vs. p distribution. For that, electrons candidates are required to fall into the $n\sigma_e^{\mathrm{TPC}}$ range of -1.5 to 3, independent of momentum. The cut is asymmetric since the pion band lies below the electron band, hence the selected $n\sigma_e^{\mathrm{TPC}}$ range must be narrower for negative values.

Besides the electron selection, a pion rejection is needed since the separation power between electrons and pions is momentum dependent. A simple electron inclusion cut

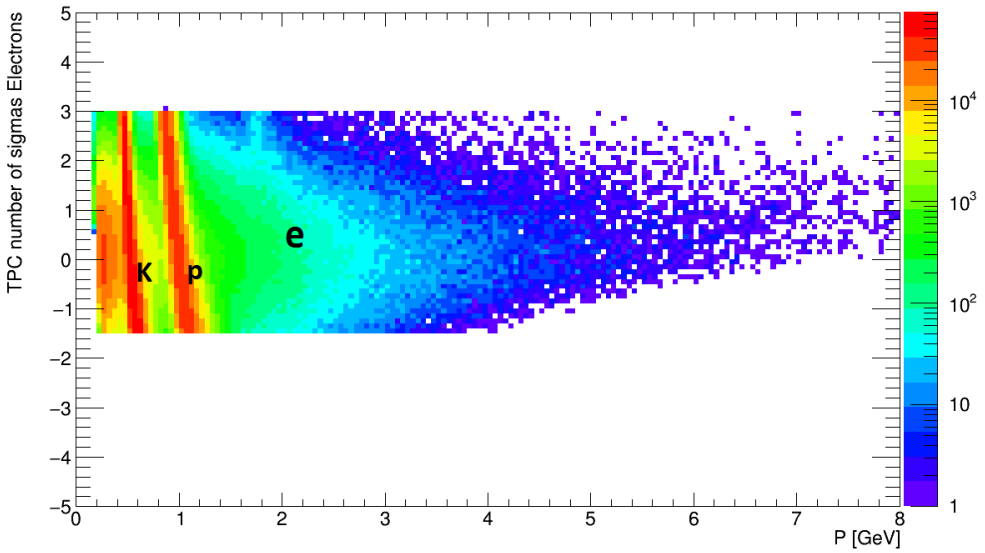

Figure 3.1: $n\sigma_e^{\mathrm{TPC}}$ distribution as a function of p after an electron inclusion cut in $-1.5 < n\sigma_e^{\mathrm{TPC}} < 3$ and pion rejection in $n\sigma_\pi^{\mathrm{TPC}} < 4$.

would then leave a big amount of contamination in the momentum ranges where the electron and pion bands merge. Hence, pions are rejected independent of momentum for $n\sigma_\pi^{\mathrm{TPC}} < 4$. The resulting $\mathrm{n}\sigma_e^{\mathrm{TPC}}$ distribution is shown in figure 3.1 as a function of momentum up to 8 GeV/c. The effect of the pion rejection can be seen for $p \gtrsim 4$ GeV/c since for $n\sigma_e^{\mathrm{TPC}} < 0$ entries are missing in the histogram. As one can see, also for smaller momenta most of the pions have been removed. However, the selected electron sample still contains kaons and protons, as the bands of these particles cross the electron band for $p \approx 0.6$ GeV/c and $p \approx 1$ GeV/c, respectively. This means, cutting only on TPC does not allow distinguishing electrons from kaons and protons in all momentum ranges.

Therefore, the additional information provided by the TOF detector has to be used. As shown in figure 3.2, using $n\sigma_e^{\mathrm{TOF}}$ can achieve a good separation of electrons from kaons and protons. The distribution shown there is obtained after applying a TPC cut as explained before. A TOF cut can be applied as well in order to reject kaons and protons. For that, the $n\sigma_e^{\mathrm{TOF}}$ range from -3 to 3 is selected in the momentum range 0.4 to 5 GeV/c. This range is chosen because above 5 GeV/c the particle bands merge not allowing PID anymore, as can be seen in figure 2.7, while for momenta below 0.4 GeV/c the electrons either do not reach the TOF detector or they reach it with a very small inclination angle with respect to its surface, which leads to a high probability of fake matches. The resulting $n\sigma_e$ distributions of the

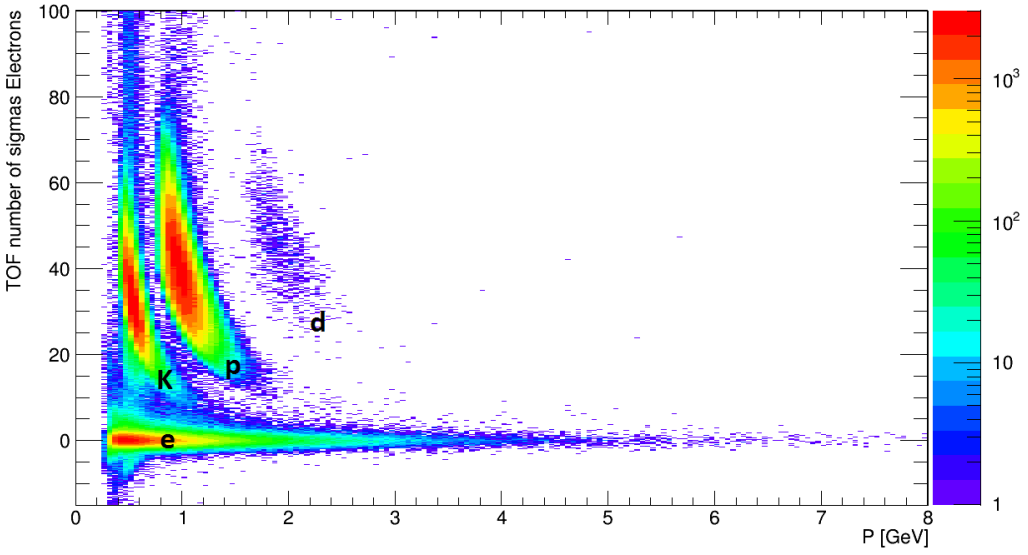

Figure 3.2: $n\sigma_e^{\mathrm{TOF}}$ distribution as a function of p after a TPC cut in $-1.5 < n\sigma_e^{\mathrm{TPC}} < 3$ and pion rejection in $n\sigma_\pi^{\mathrm{TPC}} < 4$.

TOF and TPC detectors after these selection criteria are shown as a function of p in figure 3.3.

In the combined TPC/TOF cut, it was required to always have a hit in TOF. This means that, since not for all tracks a match in TOF can be found, the tracks reconstructed only by the TPC are rejected, which leads to the elimination of $\approx 50\%$ of the found electron candidates. An alternative to this, is to require the TOF signal only if a good match has been found. In the case that no TOF match is found, the track is not rejected but a default time-of-flight $t_{\mathrm{TOF}} = 99\,999$ ps is assigned to the particle. This leads to a value of $\beta \approx 0.2$, which corresponds to the band made of particles that do not have a match in TOF in the β vs. p distribution shown in figure 3.4. Since this band is more than 100σ away from the electrons, it does not affect the electron identification after a TOF cut. Combined with a TOF 'if available' cut, the ITS signal has to be used to discriminate the particles that were not matched in the TOF detector. The ITS can be used to improve the particle identification since the kaon and proton bands cross the electron band at other momenta than in the TPC due to a different detector material, which leads to different energy loss curves. Hence, the third cut combination is called ITS/TPC/TOFif. The TPC and TOF cuts remain the same as for the previous one (except that the TOF signal is required only if available). On the ITS, a cut is applied in the $n\sigma_e^{\mathrm{ITS}}$ range from -5 to 1 for the whole momentum range ($0.2 < p < 100$ GeV/c). As it can be seen in figure 3.5,

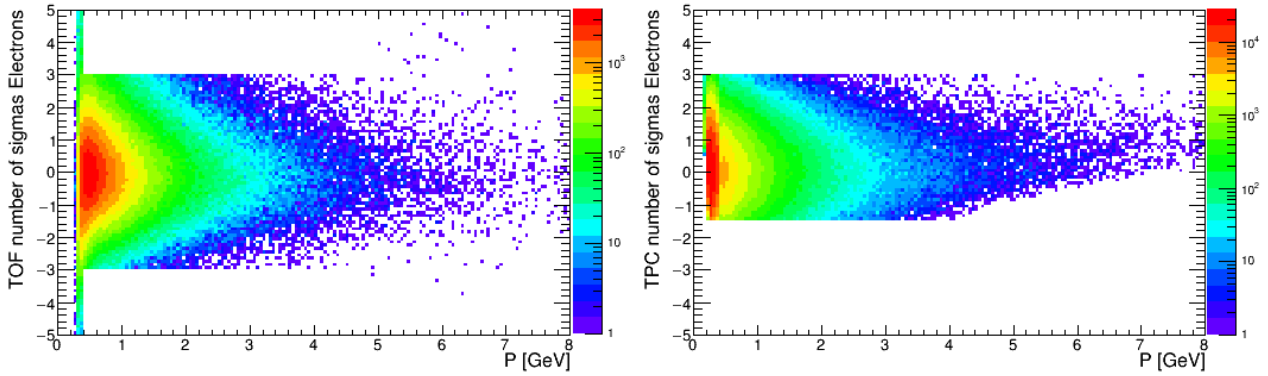

(a) TOF (b) TPC

Figure 3.3: TOF and TPC $n\sigma_e$ distributions as a function of p after a TPC cut in $-1.5 < n\sigma_e^{\mathrm{TPC}} < 3$ and pion rejection in $n\sigma_\pi^{\mathrm{TPC}} < 4$, and a TOF cut in $-3 < n\sigma_e^{\mathrm{TOF}} < 3$ for $0.4 < p < 5$ GeV/c.

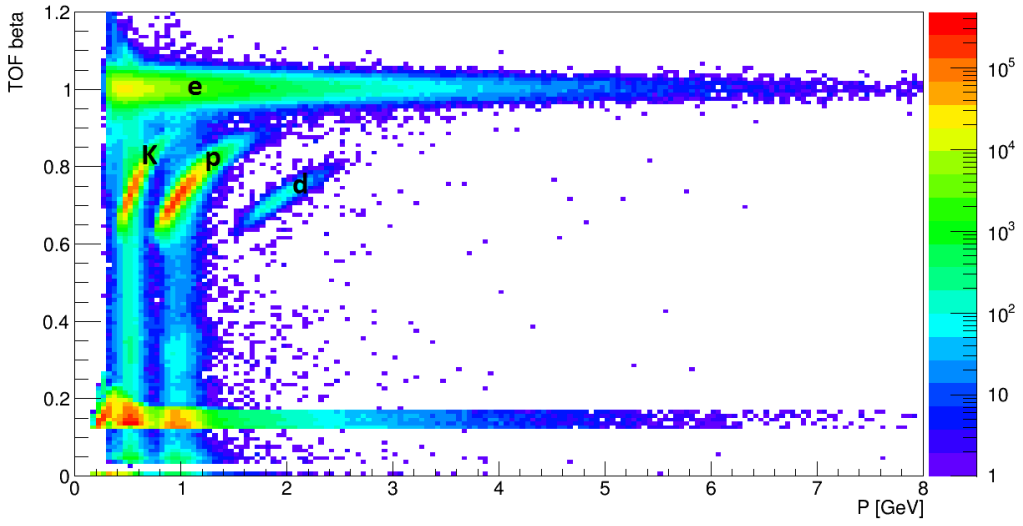

Figure 3.4: TOF β distribution as a function of p. The band at $\beta \approx 0.2$ is due to tracks that get a default value of $t_{\mathrm{TOF}} = 99\,999$ ps when no TOF match is available.

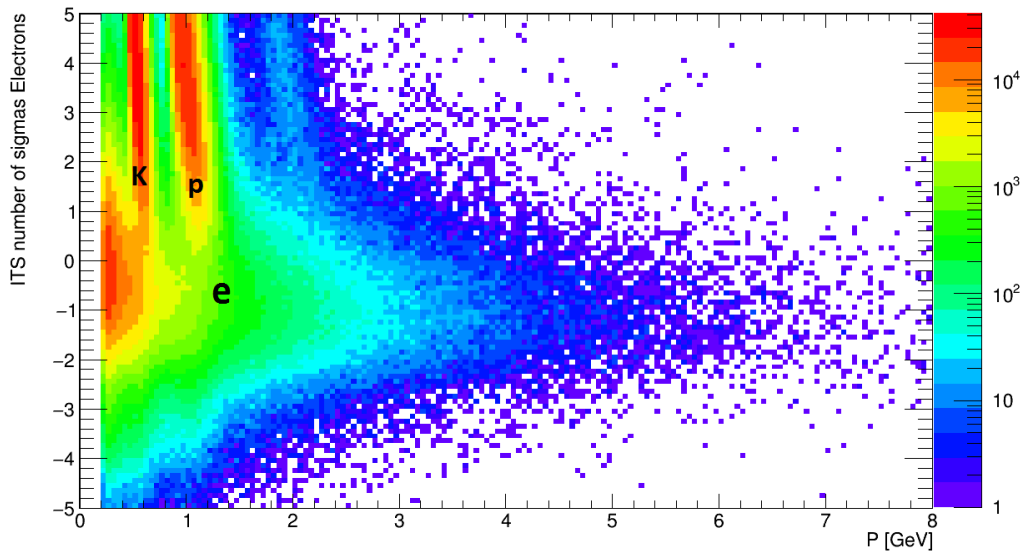

Figure 3.5: $n\sigma_e^{\mathrm{ITS}}$ distribution as a function of p after a TPC cut in $-1.5 < n\sigma_e^{\mathrm{TPC}} < 3$ and pion rejection in $n\sigma_\pi^{\mathrm{TPC}} < 4$. A cut in $-5 < n\sigma_e^{\mathrm{ITS}} < 1$ can remove most of the kaons and protons.

which shows the $n\sigma_e^{\mathrm{ITS}}$ distribution as a function of p after a TPC cut, this allows the rejection of most of the kaons and protons. The resulting $n\sigma_e$ distributions for all three detectors after the ITS/TPC/TOFif cut are shown in fig. 3.6.

As it can be seen in figure 3.5, below 0.4 GeV/c no hadron band is crossing the electron band, i.e. the selected $n\sigma_e^{\mathrm{ITS}}$ range could be extended up to 3σ in this momentum region. This is done for the fourth cut combination considered in this work, i.e. the TPC and TOF cuts remain the same as in the ITS/TPC/TOFif cut described before, but the ITS cut is modified: the range $-5 < n\sigma_e^{\mathrm{ITS}} < 3$ is selected for $0.2 < p < 0.4$ GeV/c, while above 0.4 GeV/c the cut is applied already at 1σ as before. The resulting $n\sigma_e$ distributions for all three detectors after this cut are shown in fig. 3.7.

For a better overview, these four PID sets that are the basis of the analysis following in the next sections are summarized in table 3.1.

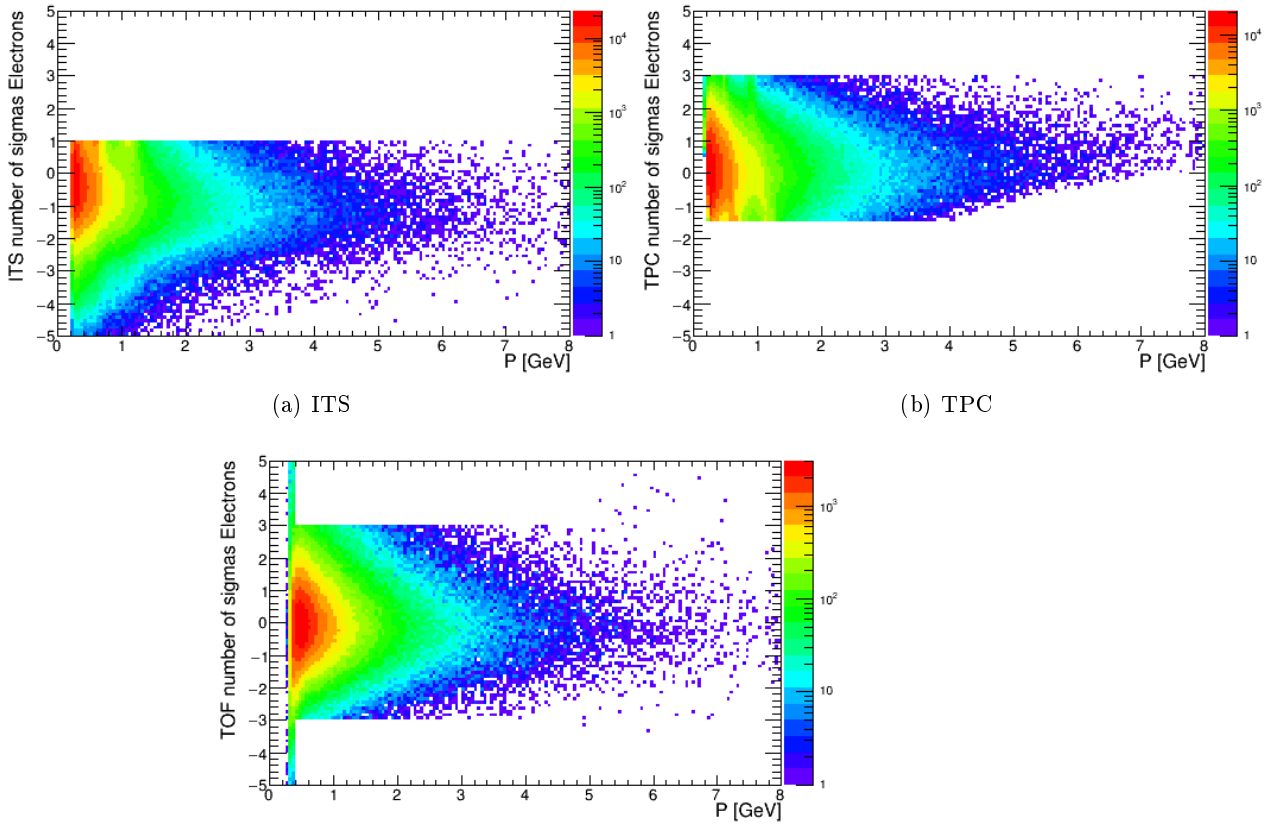

(a) ITS

(b) TPC

(c) TOF

Figure 3.6: ITS, TPC and TOF $n\sigma_e$ distributions as a function of p after a TPC cut in $-1.5 < n\sigma_e^{\mathrm{TPC}} < 3$ and pion rejection in $n\sigma_\pi^{\mathrm{TPC}} < 4$, a TOF cut in $-3 < n\sigma_e^{\mathrm{TOF}} < 3$ for $0.4 < p < 5$ GeV/c (only if available), and an ITS cut in $-5 < n\sigma_e^{\mathrm{ITS}} < 1$.

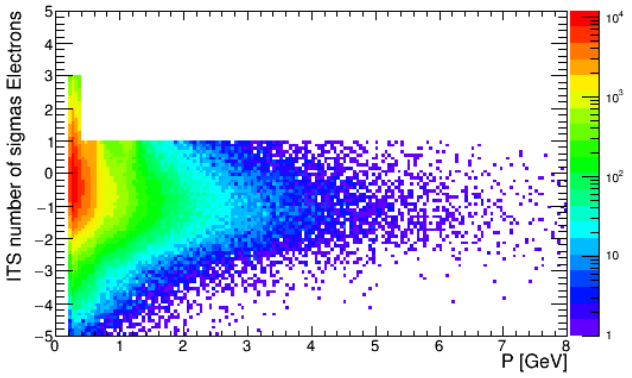

(a) ITS

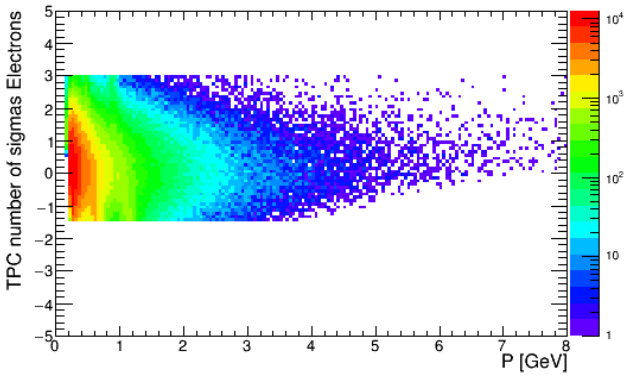

(b) TPC

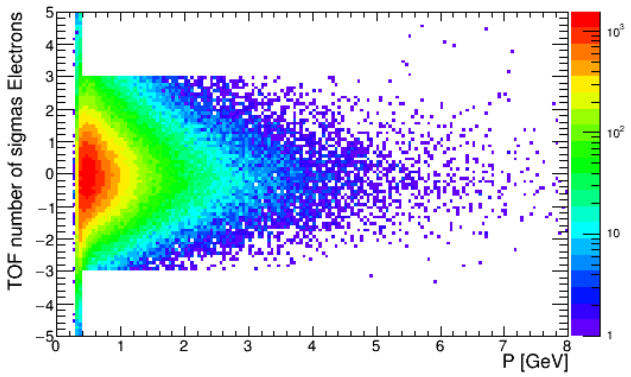

(c) TOF

Figure 3.7: ITS, TPC and TOF $n\sigma_e$ distributions as a function of p after a TPC cut in $-1.5 < n\sigma_e^{\mathrm{TPC}} < 3$ and pion rejection in $n\sigma_\pi^{\mathrm{TPC}} < 4$, a TOF cut in $-3 < n\sigma_e^{\mathrm{TOF}} < 3$ for $0.4 < p < 5$ GeV/c (only if available), and an ITS cut in $-5 < n\sigma_e^{\mathrm{ITS}} < 3$ for $0.2 < p < 0.4$ GeV/c and $-5 < n\sigma_e^{\mathrm{ITS}} < 1$ for $p > 0.4$ GeV/c.

	ITS		TPC		TOF	
applied cut	$n\sigma_e^{\mathrm{ITS}}$	p (GeV/c)	$n\sigma_e^{\mathrm{TPC}}$	p (GeV/c)	$n\sigma_e^{\mathrm{TOF}}$	p (GeV/c)
TPC only	—	—	−1.5 – 3	0.2 – 100	—	—
TPC TOF	—	—	−1.5 – 3	0.2 – 100	−3 – 3	0.4 – 5
ITS TPC TOFif	−5 – 1	0.2 – 100	−1.5 – 3	0.2 – 100	−3 – 3	0.4 – 5
ITSmod TPC TOFif	−5 – 3	0.2 – 0.4	−1.5 – 3	0.2 – 100	−3 – 3	0.4 – 5
	−5 – 1	0.4 – 100				

Table 3.1: PID sets for electron identification.

3.2 Electron Pair Analysis

Since in electromagnetic decays electrons are always produced in pairs, like in the decay of the ρ hadron: $\rho \rightarrow e^+e^-$, a pair analysis aims to identify the origin of electrons. As in an event several e^+e^- pairs are produced from different decays, the source of each electron is a priori unknown. Therefore, each electron has to be combined with all other electrons coming from the same event. In this way, one obtains three different distributions: all e^+e^- pairs, N_{+-}, and two like-sign pairs, N_{++} and N_{--}. The N_{+-} distribution is then composed of physical and combinatorial pairs. The physical pairs can be only of unlike-sign type. They originate from hadron decays, photon conversions or correlated semileptonic charm and bottom decays. This last source produces e^+e^- pairs that do not come from the same particle, but are correlated through flavor conservation. Therefore, they are considered physical pairs. The combinatorial pairs can be both like-sign and unlike-sign and are the result of the combination of each electron with all other electrons of the same event, i.e. they are not correlated. Hence, the like-sign spectra, N_{++} and N_{--}, contain no physics information and give a direct measure of the combinatorial background.

From the single track information, the transverse momentum of the pair and the invariant mass m_{ee} can be determined as follows:

$$\vec{p}_{T,ee} = \vec{p}_{T,+} + \vec{p}_{T,-} \tag{3.1}$$

$$m_{ee}^2 = (p_+ + p_-)^2 = (E_+ + E_-)^2 - (\vec{p}_+ + \vec{p}_-)^2\,, \tag{3.2}$$

with $E_\pm = \sqrt{\vec{p}_\pm^2 + m_e^2}$, $m_e = 511$ keV$/c^2$ the electron mass, $\vec{p} = (p_x, p_y, p_z) = (p_T\cos\phi, p_T\sin\phi, p_T\cot\theta)$ the electron momentum vector, which is determined by the measured quantities p_T, ϕ and θ.

3.2.1 Signal and Background Estimation

For each PID set introduced in 3.1.2, the distribution of all e^+e^- pairs, N_{+-}, is studied as a function of invariant mass, integrated over all pair p_T. Since these spectra contain also the combinatorial unlike-sign pairs, i.e. unlike-sign background (B_{+-}), a method has to be used to describe this combinatorial background. B_{+-} is therefore estimated from the geometric mean of the like-sign pairs distributions, N_{++} and N_{--}:

$$B_{+-} = 2\sqrt{N_{++}N_{--}} \tag{3.3}$$

For a proper description of the background, a correction factor has to be applied to formula 3.3 because of the different acceptance for like- and unlike-sign pairs in the central-barrel detectors. This is due to the fact that positively and negatively charged particles are bent in opposite directions by the magnetic field. Hence, the

different charge combinations will be lost at different kinematic configurations due to detector acceptance effects. For this correction, the mixed events can be used, since they preserve the acceptance difference between like- and unlike-sign pairs. The event mixing method consists of combining electrons from different events to pairs, which are then by definition uncorrelated. This can be done with many events to describe the mixed event spectrum with negligible statistical uncertainties. Again, both like- and unlike-sign pair distributions are considered: M_{+-}, M_{++} and M_{--}. The acceptance correction factor R is then the ratio of the unlike-sign pairs distribution and the geometrical mean of the like-sign pairs distributions:

$$R = \frac{M_{+-}}{2\sqrt{M_{++}M_{--}}}. \tag{3.4}$$

Hence, the complete description of the background is obtained multiplying the unlike-sign background from real events, B_{+-}, by the R factor from mixed events:

$$B = B_{+-} \cdot R = \sqrt{N_{++}N_{--}} \cdot \frac{M_{+-}}{\sqrt{M_{++}M_{--}}}. \tag{3.5}$$

This method, that makes use of both real and mixed events, has to be applied since $M_{+-} \neq B_{+-}$. This is due to the fact that some e^+e^- pairs can be correlated even if they do not come from the same parent particle, in the case that one of the pairs and the source of the other pair originated from the same particle, i.e. the electrons have the same grandparent. This can be easily understood looking at the Dalitz decay of a neutral pion: $\pi^0 \rightarrow \gamma\ e^+e^-$. As the photon can convert to an e^+e^- pair, the electrons of this decay are correlated with the electrons of the direct Dalitz decay, since the total mass must be smaller than the pion mass. In mixed events, however, the correlation is lost. Therefore, the mixed events unlike-sign pairs distribution cannot be directly used to describe the background.

Subtracting the total background B from the distribution of all unlike-sign pairs from real events, i.e. N_{+-}, the physical signal S is obtained:

$$S = N_{+-} - B \tag{3.6}$$

The unlike-sign pair, background and signal spectra are shown for all four cuts in figure 3.8. As can be seen, the spectra have a similar trend for all cuts, with the combinatorial background always being the main contribution to the N_{+-} spectrum. A small peak can be seen for all four cuts in the mass bin from 3 to 3.2 GeV/c^2. This region corresponds to the J/ψ meson, which has a mass of 3.096 GeV/c^2 and decays into a e^+e^- pair with a branching fraction of $\approx 6\%$ [13]. The ω and ϕ mesons, with $m = 0.782$ and $m = 1.019$ GeV/c^2 [13] respectively, cannot be seen as a peak because of the big underlying continuum.

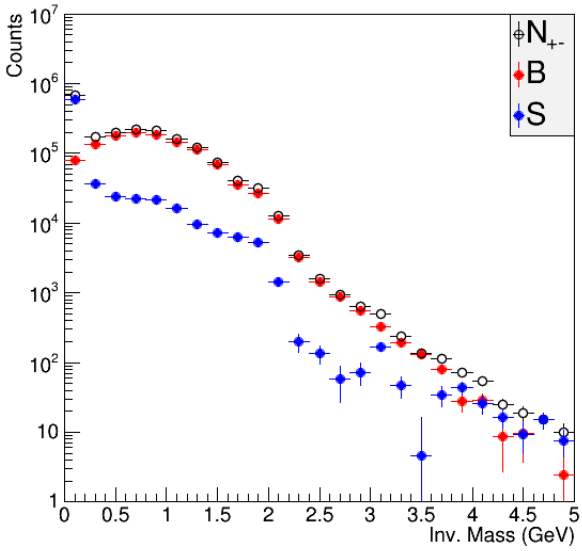

(a) TPC selection

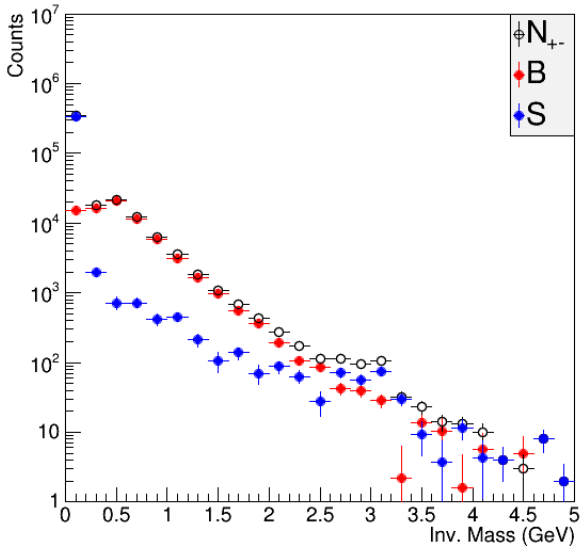

(b) TPC-TOF selection

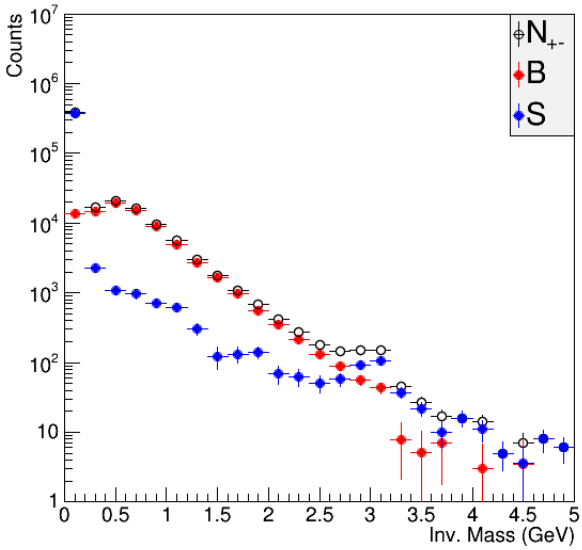

(c) ITS-TPC-TOFif selection

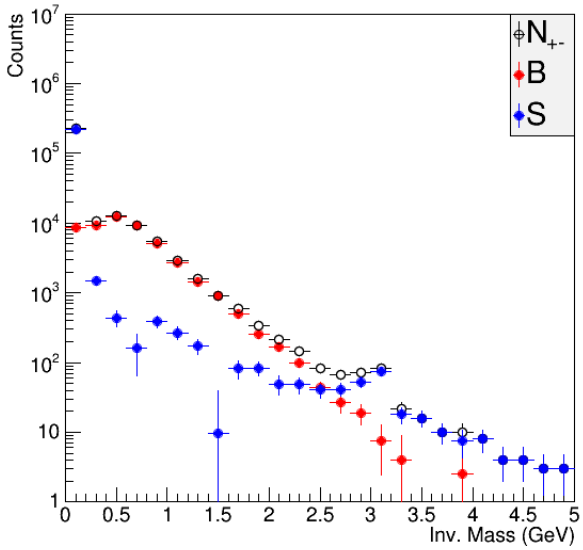

(d) ITSmod-TPC-TOFif selection

Figure 3.8: Unlike-sign pair (N_{+-}), background (B) and signal (S) spectra as a function of invariant mass for all four selection criteria.

Mass regions in GeV/c^2	Main dielectron source
$m_{ee} < 0.1$	π^0 Dalitz decay
$0.1 < m_{ee} < 0.3$	η Dalitz and γ^* decay (in heavy ions)
$0.3 < m_{ee} < 0.7$	modifications of ρ meson
$0.7 < m_{ee} < 1.2$	ρ, ω and ϕ
$1.2 < m_{ee} < 2.8$	charm decays and thermal dielectrons (in heavy-ions)
$2.8 < m_{ee} < 3.2$	J/ψ
$m_{ee} > 3.2$	semileptonic bottom decays

Table 3.2: Main dielectron sources and corresponding invariant mass regions used to rebin the unlike sign pair, background and signal spectra.

To reduce statistical fluctuations, the spectra shown in figure 3.8 can be rebinned according to some specific invariant mass regions, where the production or the decay of a particular particle is expected: below 0.1 GeV/c^2 the main dielectron source is the π^0 Dalitz decay, in the mass region between 0.1 and 0.3 GeV/c^2 thermal radiation, i.e. the decay of virtual photons γ^*, is expected to contribute significantly in heavy-ion collisions on top of η Dalitz decays, between 0.3 and 0.7 GeV/c^2 modifications of the ρ meson are expected, for $0.7 < m < 1.2$ GeV/c^2 dielectron pairs come from decays of ρ, ω and ϕ mesons, in the continuum region between 1.2 and 2.8 GeV/c^2 the main sources are thermal dielectrons in heavy-ion collisions and semileptonic decays of charm mesons, between 2.8 and 3.2 GeV/c^2 electrons come from the decay of the J/ψ meson, and above 3.2 GeV/c^2 semileptonic decays of bottom mesons give the main contribution to electron pair production. The mass regions are summarized in table 3.2. After rebinning the unlike-sign pair, background and signal spectra are divided by the respective bin width and are shown for all four cuts in figure 3.9.

3.2.2 Signal to Background Ratio and Statistical Significance

For a proper comparison of the different PID sets, the ratio of signal and background as well as the significance of the signal, S/σ_S (with σ_S the statistical uncertainty on S), are studied as a function of invariant mass. The mass rebinning introduced in the previous section was used again to get a non-fluctuating estimate of these distributions.

The S/B ratio is relevant for the systematic uncertainty on mixed events normalization, if they were to be directly subtracted from the N_{+-} distribution to obtain the signal. In this case, the background is given from the mixed events unlike-sign pairs distribution, M_{+-}, multiplied by a normalization factor, α, needed since for

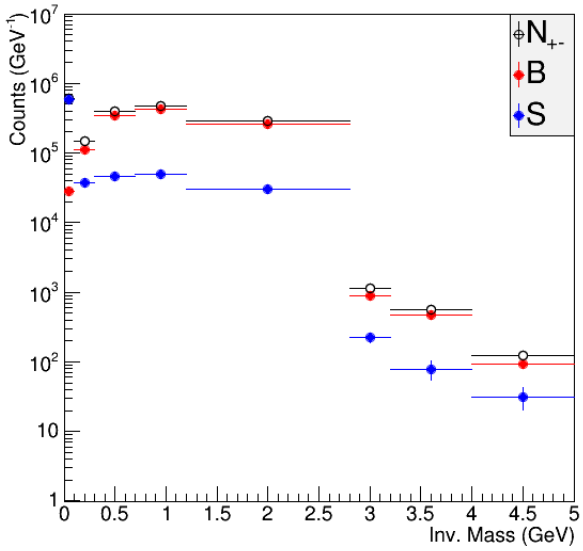

(a) TPC selection

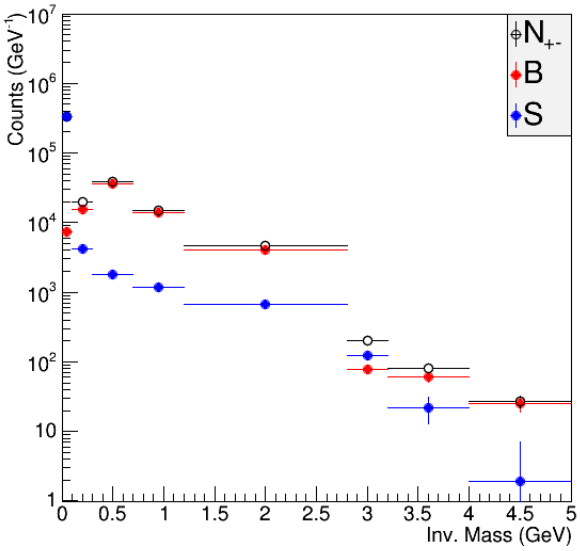

(b) TPC-TOF selection

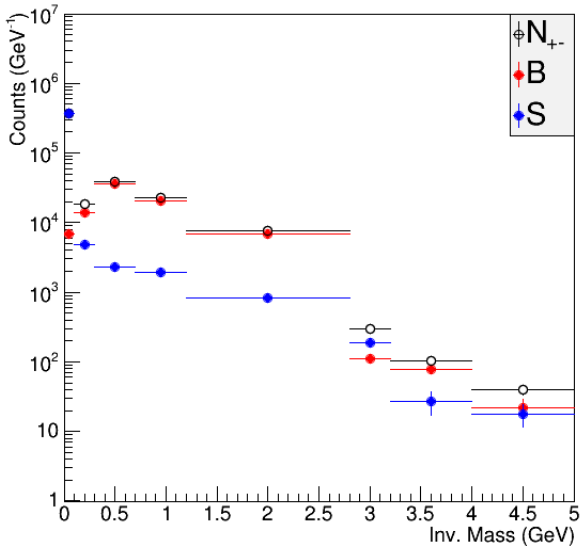

(c) ITS-TPC-TOFif selection

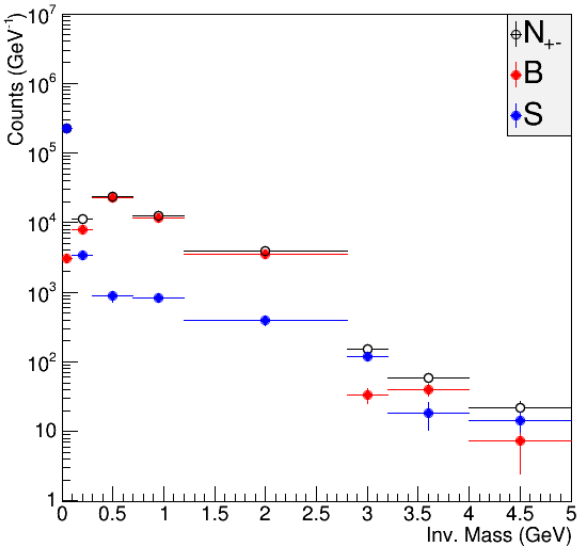

(d) ITSmod-TPC-TOFif selection

Figure 3.9: Unlike-sign pair (N_{+-}), background (B) and signal (S) spectra for all four selection criteria after mass rebinning according to table 3.2.

each real event many mixed events are created:

$$B = \alpha\ M_{+-} \tag{3.7}$$
$$\Longrightarrow S = N_{+-} - \alpha\ M_{+-} = N_{+-} - B \tag{3.8}$$

Since the absolute systematic uncertainty due to the background normalization on the signal is equal to the one of the background ($\Delta S = \Delta B$), the relative error of the signal becomes:

$$\frac{\Delta S}{S} = \frac{\Delta B}{S} = \frac{\Delta B}{B} \cdot \frac{B}{S}, \tag{3.9}$$

i.e. the relative error on the background divided by S/B. Hence, a small S/B ratio leads to a high uncertainty on the signal. The S/B distribution as a function of invariant mass is shown for all four PID cuts in figure 3.10 up to S/B = 1 (for $m_{ee} > 3$ and $m_{ee} < 0.1$ GeV/c^2 not all four PID cuts can be seen as some of them have a bigger S/B value). This is the most interesting region, since for S/B > 1 the typical relative error of the signal is negligible. However, as it can be seen, the distributions fluctuate despite the mass rebinning not allowing to make a clear statement about which PID set has the best S/B ratio.

The significance is the inverse of the relative statistical uncertainty on the signal (σ_S/S). Since the N_{+-} and B mass spectra contain count rates that are described by Poisson distributions, their statistical uncertainties are given by the square-root of the yields:

$$\sigma_{N_{+-}} = \sqrt{N_{+-}} = \sqrt{S+B};$$
$$\sigma_B = \sqrt{B}. \tag{3.10}$$

The signal statistical uncertainty is then given by the quadratic sum of the errors on N_{+-} and B:

$$\sigma_S = \sqrt{\sigma^2_{N_{+-}} + \sigma^2_B} = \sqrt{(S+B)+B} = \sqrt{S+2B}, \tag{3.11}$$

so that for the statistical significance one obtains:

$$\frac{S}{\sigma_S} = \frac{S}{\sqrt{S+2B}}. \tag{3.12}$$

The significance as a function of invariant mass is shown for all four PID cuts in figure 3.11.

The distributions clearly show that the TPC-only cut yields the largest S/σ_S ratio in almost all invariant mass bins. Hypothetically, the PID set with the higher significance is the most appropriate to identify electrons, but in figure 3.1 it can already be seen that, after applying a cut only on the $n\sigma_e^{\mathrm{TPC}}$ vs. p distribution, the

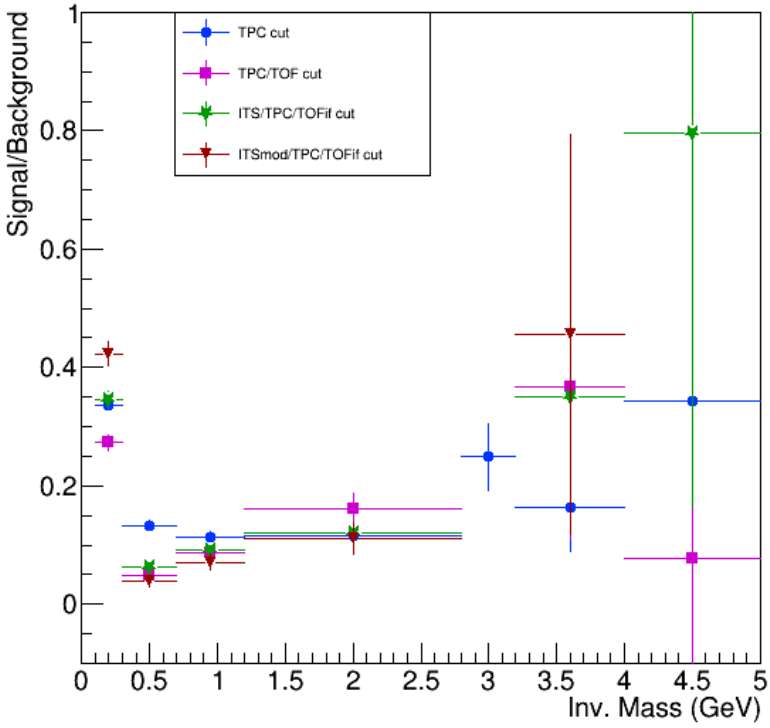

Figure 3.10: S/B ratio as a function of invariant mass for all four PID cuts.

selected electron sample still contains a big amount of kaons and protons that are considered as electrons in the pair analysis biasing the signal.

After the TPC cut, the PID set with the highest significance is the ITS/TPC/TOFif one. However, it is important again to take into account the contamination of the signal that comes from hadrons misidentified as electrons, since the like-sign mass spectra do not completely eliminate these hadrons from the unlike-sign spectrum. This happens, if hadrons are produced in resonance decays as unlike-sign pairs. For example, consider the decays of a ρ meson in two pions ($\rho \to \pi^+\pi^-$) and of an η meson in three pions ($\eta \to \pi^0\pi^+\pi^-$). If the charged pions are misidentified as electrons, the subtraction of the like-sign background would eliminate two pairs made of one pion coming from the ρ decay and one from the η decay, but the other two combinations, i.e. the two pairs of pions coming from the same decay, would be handled as signal.

Therefore, a contamination study is performed for the TPC and ITS/TPC/TOFif cuts and discussed in the following sections.

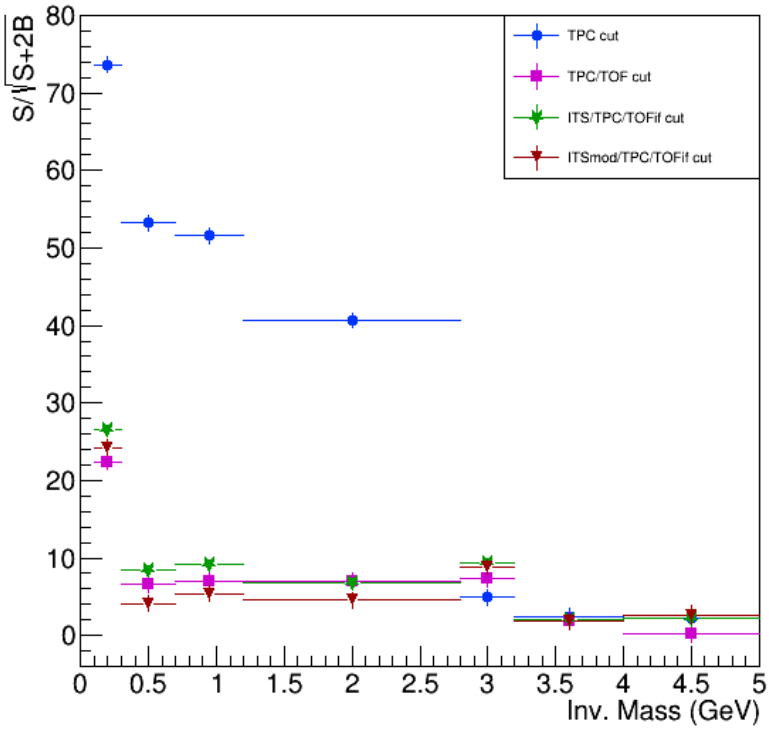

Figure 3.11: Statistical significance S/σ_S as a function of invariant mass for all four PID cuts.

3.3 Signal Purity Studies

3.3.1 TOF-based Approach

The contamination of the TPC-only cut cannot be estimated using the $n\sigma_e^{\mathrm{TPC}}$ vs p distribution since, as can be seen in figure 3.1, the kaons and protons cannot be separated from the electrons in the selected $n\sigma_e^{\mathrm{TPC}}$ and p ranges, i.e. it is impossible to know how big the fraction of hadrons contained in the selected electron sample is. To do that, the $n\sigma_e^{\mathrm{TOF}}$ vs p distribution after applying a TPC cut has to be considered, since it provides a very good separation of electrons from kaons and protons, as shown in figure 3.2.

For the hadron contamination estimation, this distribution is studied in intervals of 0.1 GeV/c for $0.4 < p < 1.2$ GeV/c. For momenta bigger than 1.2 GeV/c much less data are available, hence it is not possible to study the distribution in such narrow

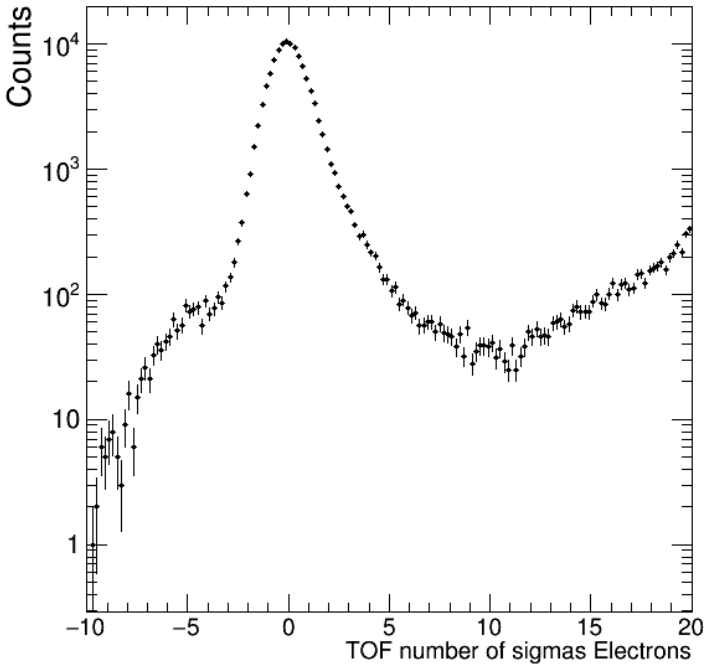

Figure 3.12: $n\sigma_e^{\mathrm{TOF}}$ spectrum integrated in the momentum range $0.5 < p < 0.6$ GeV/c.

momentum ranges. Instead, the intervals 1.2 – 1.4, 1.4 – 1.6, 1.6 – 2 and 2 – 8 GeV/c are considered. For each momentum range, the distribution is fitted by a model in order to understand the background contained in the electron sample. After the fit, the contamination can be extracted for each momentum interval. For convenience, the purity of the electron sample is determined instead of the contamination, which however is connected to the latter in a very simple way, since the sum of the two quantities is equal to 1, by construction. The determined purity is the average of the electron and positron purities.

The $n\sigma_e^{\mathrm{TOF}}$ spectrum, obtained after integrating over momentum for $0.5 < p < 0.6$ GeV/c, is shown in figure 3.12 up to $20\sigma_e^{\mathrm{TOF}}$. As it can be seen, the electrons are centered at zero, while the kaon and proton peaks are not visible since they are more than 20σ separated from the electron signal (note however that the separation power is momentum dependent). The biggest source of contamination at low momenta are fake matches of tracks from the TPC to the TOF signal, i.e., in figure 3.12, the wide plateau under the electron peak. Fake matches can also clearly be seen in the β vs. p distribution (figure 3.4): they correspond to the data outside the expected particle bands and are independent of the velocity. To extract the purity of the electron sample for $0.5 < p < 0.6$ GeV/c, the distribution shown in figure 3.12 has to be fitted.

For that, the signal, i.e. the electron peak, and the background, i.e. the plateau under the peak (or for higher momenta the hadron peaks), are first fitted separately with two different functions since this allows to find the best fit parameters to describe them. But first, an initial assumption has to be made for the fit shape. As it can be seen in figure 3.12, the electron peak is not a perfect Gaussian, but has a tail on the right side. This is due to a not optimal parametrization of the TOF β distribution and the fact that electrons can lose energy via bremsstrahlung while traversing the ITS and TPC detectors. Because of this energy loss the electrons slow down and their time-of-flight increases compared to the momentum which is measured before the energy loss. Therefore, to describe the electron signal an inverse Crystal ball function is chosen, given by the following formula:

$$f(x, \bar{x}, \sigma, \alpha, n) = \begin{cases} \exp\left(-\frac{(x-\bar{x})^2}{2\sigma^2}\right), & \frac{x-\bar{x}}{\sigma} < \alpha \\ A \cdot \left(B + \frac{x-\bar{x}}{\sigma}\right)^{-n}, & \frac{x-\bar{x}}{\sigma} > \alpha \end{cases} \tag{3.13}$$

where

$$A = \left(\frac{n}{|\alpha|}\right)^n \cdot \exp\left(-\frac{|\alpha|^2}{2}\right)$$
$$B = \frac{n}{|\alpha|} - |\alpha|\,.$$

The inverse Crystal ball consists of a Gaussian with mean $\bar{x}$ and width σ, that merges into a falling power-law function at a certain x-value α. The last free parameter, n, indicates how quickly the power-law function drops. For the background, a fifth order polynomial is used in this momentum range. After fitting signal and background individually to seed the parameters, the sum of the fit functions is used to fit the whole data maximizing the loglikelihood. The fitted $n\sigma_e^{\mathrm{TOF}}$ spectrum for $0.5 < p < 0.6$ GeV/c is shown in figure 3.13. As it can be seen, the Crystal ball and the polynomial describe very well the electron signal and the underlying fake match background, respectively. The figure also shows that the electron peak has a width that is not equal to one, suggesting again that the $n\sigma_e^{\mathrm{TOF}}$ parametrization is not perfect. The quality of the fit is also confirmed by the pull distribution, which can be seen in the lower part of the figure. The pull distribution is defined as follows:

$$\frac{D-F}{\Delta D}, \tag{3.14}$$

i.e. it is the difference between data (D) and total fit function (F), divided by the error on the data (ΔD), i.e. $\sqrt{D}$. This means, it indicates how much the fit differs from the data. A fit of good quality yields a Gaussian pull distribution with mean of zero and root-mean-square of 1, i.e. with most values spread between −2 and 2.

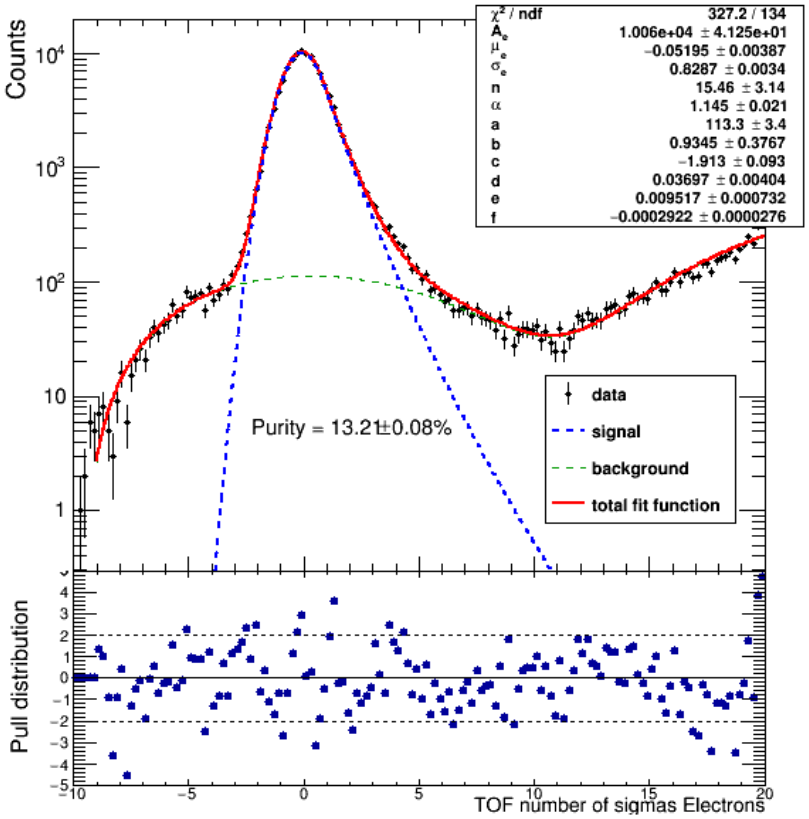

Figure 3.13: $n\sigma_e^{\mathrm{TOF}}$ spectrum for $0.5 < p < 0.6$ GeV/c, fitted with the sum of a Crystal ball function (for the electron signal) and a fifth degree polynomial (for the background). The fit reveals a contamination of 13.21% for the TPC cut in this momentum region. The pull distribution is spread between −2 and 2, indicating a good fit quality.

After fitting the $n\sigma_e^{\mathrm{TOF}}$ distribution, it is possible to determine the purity P of the electron sample as follows:

$$P = \frac{S}{F}, \tag{3.15}$$

with S the signal function integrated over the whole $n\sigma_e^{\mathrm{TOF}}$ region and F the total number of candidates. For the momentum region in figure 3.13, the purity amounts to $13.21 \pm 0.08\%$, i.e. only this fraction of the candidates selected after the TPC cut are really electrons and the rest are fake matches, kaons or protons. For higher momenta, the amount of fake matches is much smaller, but it can still be assumed that they constitute a part of the electron band. This has to be taken into account when fitting the data. Therefore, a polynomial background function is fitted under the electron

peak for all momentum ranges (where no underlying plateau can explicitly be seen under the electron peak, a zero degree polynomial is used).

Since the separation power between electrons and kaons is momentum dependent, the kaon peak gets closer to the electrons with increasing momentum. This can be clearly seen in figure 3.14: for $1.0 < p < 1.1$ GeV/c and $1.1 < p < 1.2$ GeV/c kaons are $\approx 10\sigma$ separated from the electrons and the two peaks can be fitted individually. For the kaon fit a Gaussian is used as their energy loss via bremsstrahlung is suppressed by their much larger mass. In the momentum range from 1.2 to 1.4 GeV/c however, the kaon and electron peaks fully overlap and the kaons cannot be fitted separately anymore. Therefore, another method has to be used to take this into account: it is assumed that the kaon to electron ratio does not change significantly at high momenta. It amounts to $\approx 2.2 \cdot 10^{-2}$ for $1.0 < p < 1.1$ GeV/c and to $\approx 3.2 \cdot 10^{-2}$ for $1.1 < p < 1.2$ GeV/c, a small difference for our purpose. Then, the ratio of the last momentum range is used to correct the purity for momenta higher than 1.2 GeV/c, i.e. it is subtracted from the purity value obtained from the fit.

Also the separation power between electrons and protons changes with momentum. For $1.4 < p < 1.6$ GeV/c, the proton peak lies at 20σ, for $1.6 < p < 2$ GeV/c at 15σ, and for momenta higher than 2 GeV/c it overlaps with the electron peak and cannot be fitted individually with a Gaussian anymore. This is shown in figure 3.15. Therefore, the same method as for the kaons is applied: the proton to electron ratio of the previous momentum range ($\approx 3.6 \cdot 10^{-2}$) is used to correct the purity for $p > 2$ GeV/c.

The fits of the momentum intervals not discussed here can be found in Appendix A. The purity extracted from the fits is shown as a function of momentum in figure 3.16. The statistical uncertainties on the purity are smaller than the marker size. As the figure shows, for momenta lower than 1.5 GeV/c, the purity of the electron sample selected by the TPC-only cut is very low: it lies between 2% and 40% with exception of the range $0.7 < p < 0.8$ GeV/c, where it amounts to $\approx 62\%$. These values are clearly due to the kaon band for $0.4 < p < 0.7$ GeV/c and to the proton band for $0.8 < p < 1.4$ GeV/c, as well as to fake matches, while for $0.7 < p < 0.8$ GeV/c the purity gets higher since this is the momentum interval that separates the kaon and proton bands (see fig. 3.2). For $p > 1.5$ GeV/c the electron sample shows a higher purity, which reaches its maximum for high momenta ($2 < p < 8$ GeV/c). This comes from the fact that, in the $n\sigma_e^{\mathrm{TPC}}$ vs. p distribution the kaon and proton bands merge for high p with the pion band (fig. 2.6), hence the pion rejection cut removes most of them.

The purity distribution demonstrates that the statistical significance (S/σ_S) of the TPC-only cut is that high because the signal of the selected electron sample contains a very big amount of hadrons. Hence, the TPC-only PID set is not the most appropriate to identify electrons and the TOF and ITS detectors have to be used to improve the electron identification. The purity of the ITS/TPC/TOFif cut,

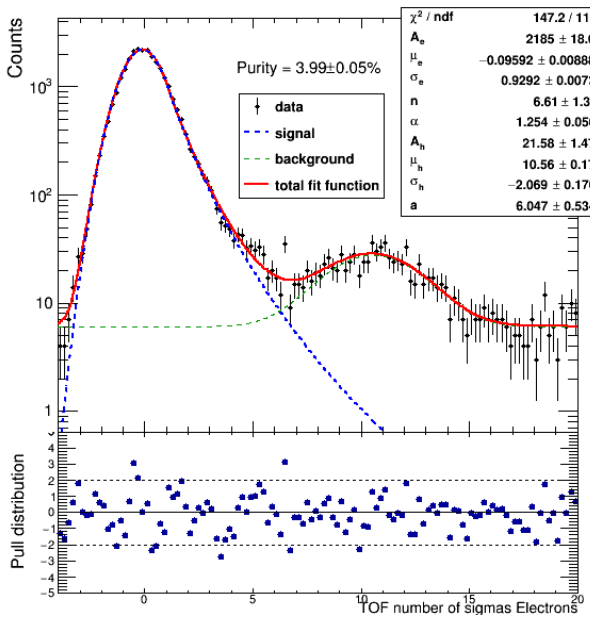

(a) $1.0 < p < 1.1$ GeV/c

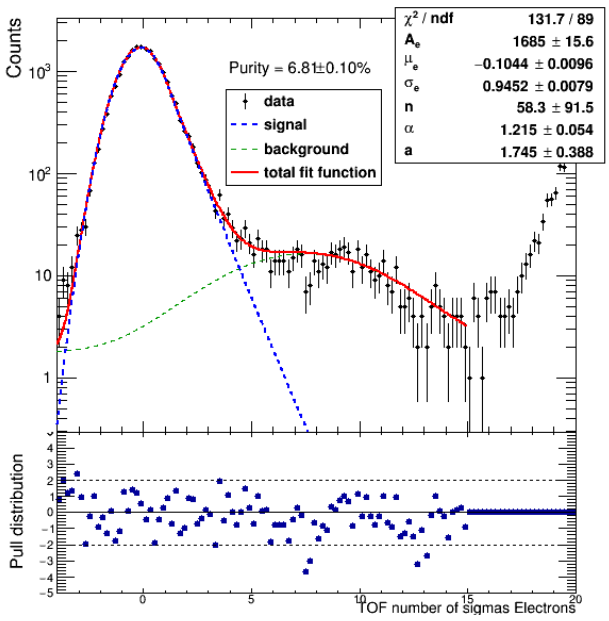

(b) $1.1 < p < 1.2$ GeV/c

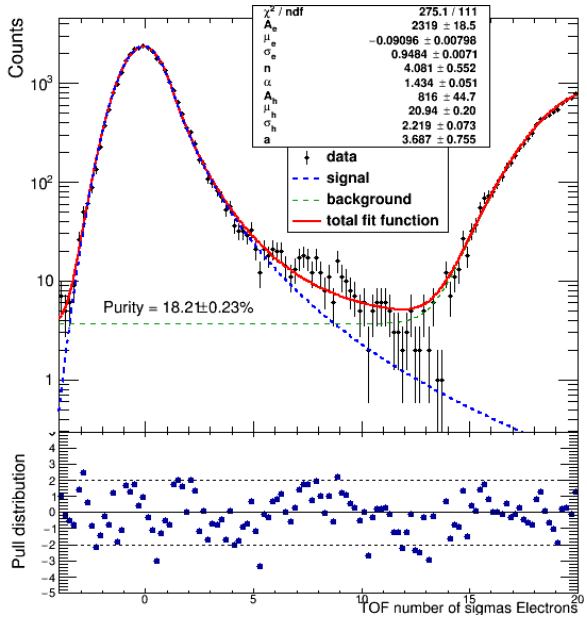

(c) $1.2 < p < 1.4$ GeV/c

Figure 3.14: $n\sigma_e^{\mathrm{TOF}}$ distributions for the momentum ranges where the kaon peak gets closer to the electron peak with increasing p, until it fully overlaps with it in c). For the purity for $p > 1.2$ GeV/c the kaon/electron ratio of the previous bin is considered.

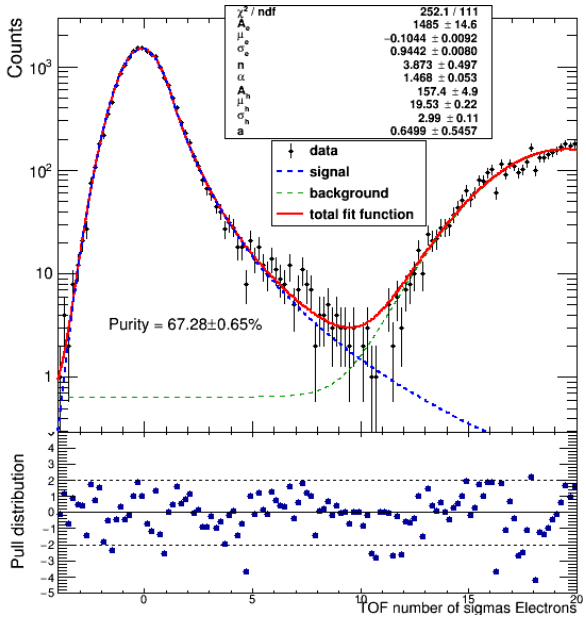

(a) $1.4 < p < 1.6$ GeV/c

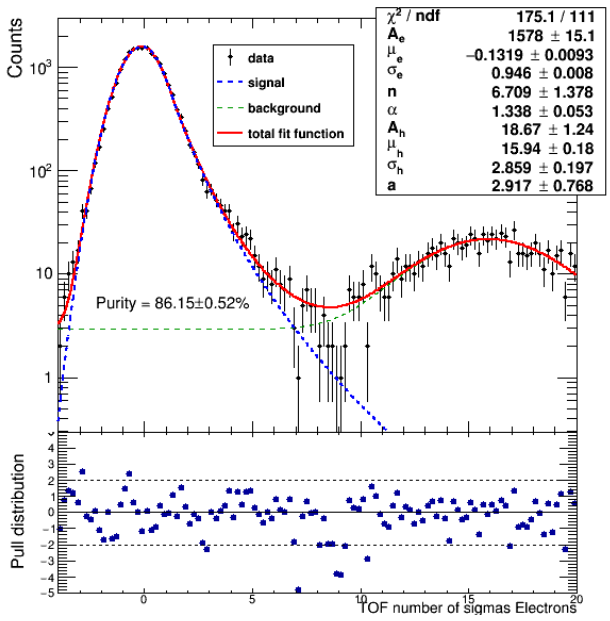

(b) $1.6 < p < 2$ GeV/c

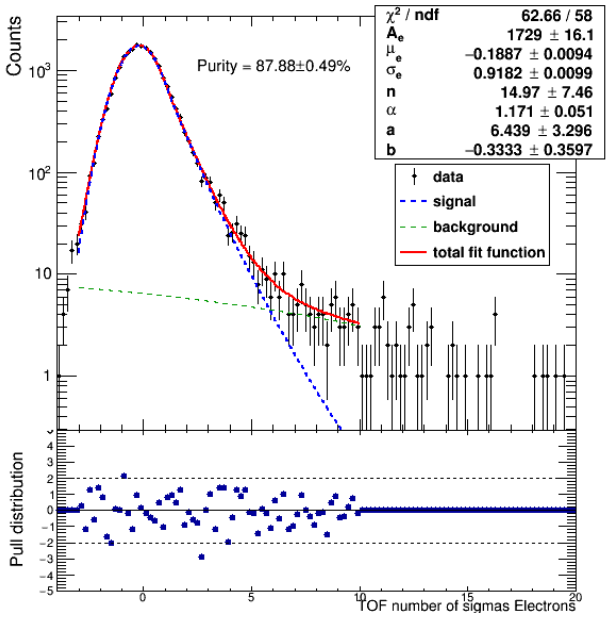

(c) $2 < p < 8$ GeV/c

Figure 3.15: $n\sigma_e^{\mathrm{TOF}}$ distributions for the momentum ranges where the proton peak gets closer to the electron peak with increasing p, until it fully overlaps with it in c). For the purity for $p > 2$ GeV/c the proton/electron ratio of the previous bin is considered.

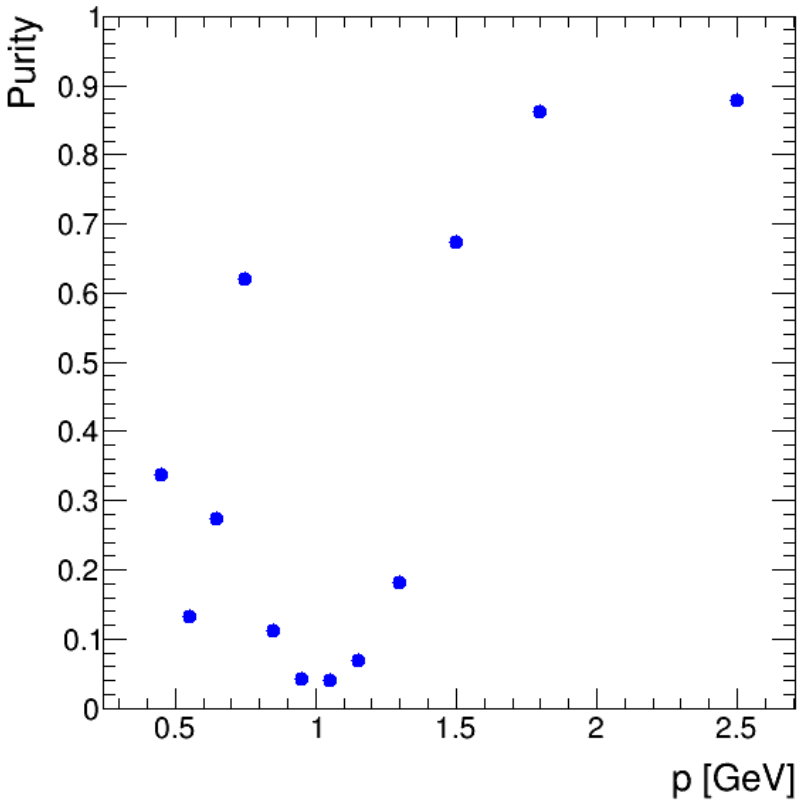

Figure 3.16: Purity of the TPC-only cut as a function of momentum.

which has the second highest significance (see fig. 3.11), is investigated in the next section.

3.3.2 TPC-based Approach

In order to determine the purity of the ITS/TPC/TOFif cut, the electron selection is applied only in the ITS and TOF, while on the TPC no cut is performed, neither electron inclusion nor pion rejection. In this way, the hadrons surviving the ITS and TOF selections are still present in the $n\sigma_e^{\mathrm{TPC}}$ distribution, as well as the hadrons that can be rejected with a TPC cut, as shown in figure 3.17. Therefore, fitting this distribution allows estimating the purity of the ITS/TPC/TOFif PID set. However, to take into account both electron inclusion and pion rejection, the $n\sigma_\pi^{\mathrm{TPC}}$ distribution has to be included in the study as well. Hence, $n\sigma_\pi^{\mathrm{TPC}}$ is considered as a function of $n\sigma_e^{\mathrm{TPC}}$, as shown in figure 3.18 integrated over all momenta. As it can be seen, the pion rejection is necessary since after an electron inclusion cut in $-1.5 < n\sigma_e^{\mathrm{TPC}} < 3$,

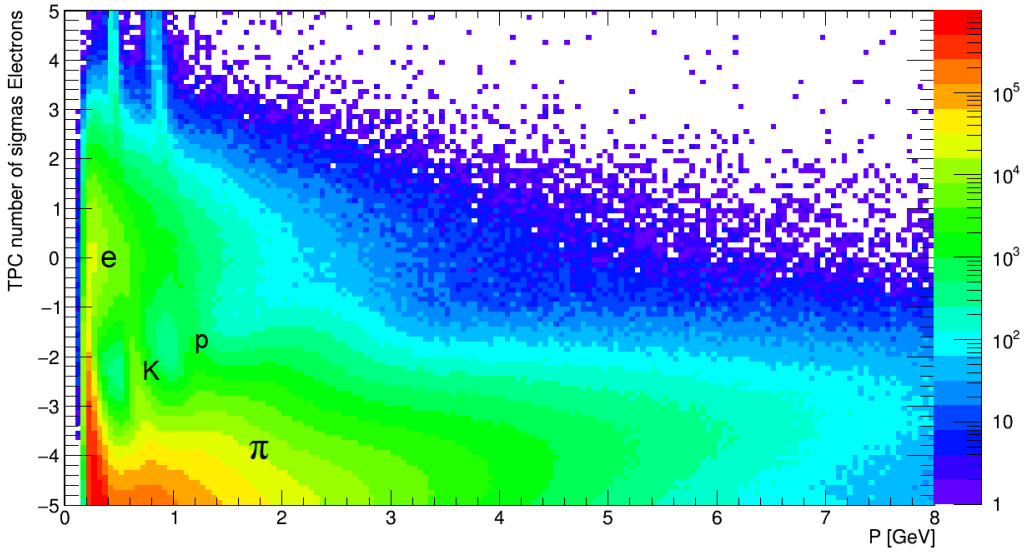

Figure 3.17: $n\sigma_e^{\mathrm{TPC}}$ distribution as a function of p after an ITS and TOFif cut. The pions, that could be rejected with a TPC cut, as well as the kaons and protons that survived the ITS and TOF cuts, are still contained in the selected sample and can be used to estimate the purity of the ITS/TPC/TOFif cut.

still some pions are left in the selected sample, in particular at high momenta. The shown distribution is considered again in momentum intervals in order to obtain the purity of the PID set as a function of p. The considered momentum ranges are the same as for the TOF fits, but since the TPC provides PID information down to 0.2 GeV/c, the ranges $0.2 < p < 0.3$ and $0.3 < p < 0.4$ GeV/c are included in the study. For each momentum interval, the distribution is projected onto the $n\sigma_e^{\mathrm{TPC}}$ axis twice: without pion rejection, i.e. integrated over all $n\sigma_\pi^{\mathrm{TPC}}$, and with pion rejection up to 4σ, i.e. for $n\sigma_\pi^{\mathrm{TPC}} > 4$. Both obtained $n\sigma_e^{\mathrm{TPC}}$ distributions are then fitted. For the fit, signal (electrons) and background (hadrons) are first fitted separately with two different functions, i.e. a Gaussian and the sum of several Gaussians or of a Gaussian and a polynomial, respectively. Then, the whole distribution is fitted with the sum of the signal and background functions maximizing the loglikelihood again. The fits allow then to determine the purity of the electron sample by dividing the electron fit function (S) by the total fit function (F), both integrated in the range $-1.5 < n\sigma_e^{\mathrm{TPC}} < 3$, since this is the interval of the electron inclusion cut in the TPC:

$$P = \frac{\int_{-1.5}^{3} S}{\int_{-1.5}^{3} F}. \tag{3.16}$$

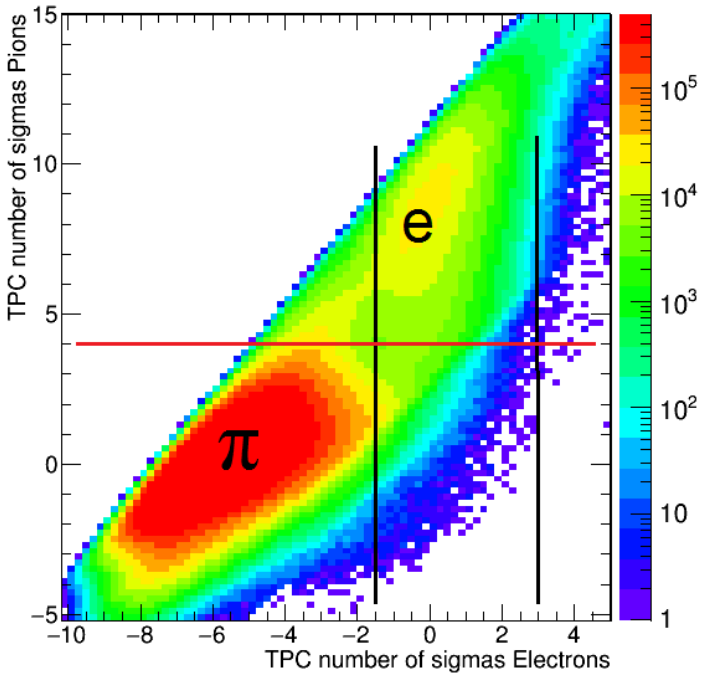

Figure 3.18: $n\sigma_{\pi}^{\mathrm{TPC}}$ vs. $n\sigma_{e}^{\mathrm{TPC}}$ distribution, integrated over momentum. The black lines indicate the electron inclusion range of the ITS/TPC/TOFif cut, while the red line shows the pion rejection cut. The distribution is studied in momentum intervals in order to determine the purity of the ITS/TPC/TOFif cut.

From the fitted distribution, also the relative efficiency ϵ of the selection for electrons can be determined. For that, the integral of the signal function for $-1.5 < n\sigma_{e}^{\mathrm{TPC}} < 3$ is divided by the integral of the signal function in the whole $n\sigma_{e}^{\mathrm{TPC}}$ range:

$$\epsilon = \frac{\int_{-1.5}^{3} S}{\int_{-\infty}^{\infty} S}. \tag{3.17}$$

Hence, the efficiency measures the quantity of electrons contained in the electron sample after the electron inclusion and the pion rejection cuts, with respect to the total number of electrons selected by ITS and TOF. However, the efficiency does not take into account the signal loss due to the pion rejection and a possible bias on the electron sample introduced by it.

In this section, only the momentum intervals are discussed where the kaon and proton bands cross the electron band in the $n\sigma_{e}^{\mathrm{TPC}}$ distribution. The remaining momentum ranges, where the determination of the purity is straightforward, can be found in Appendix B. Figure 3.19 shows the momentum ranges $0.4 < p < 0.5$,

$0.5 < p < 0.6$ and $0.6 < p < 0.7$ GeV/c, in which the kaons cross the electron band, both without pion rejection and with a $4\sigma_\pi$ cut. The effect of the pion rejection can clearly be seen: after the cut only a very small amount of pions is left. The figure also shows that all three peaks (electrons at ≈ 0, pions on the left and kaons on the right) are well described by a Gaussian, or by the sum of two Gaussians in the case of the pions (for some other momentum ranges even three). The pion peak cannot be described by a single Gaussian, since the pion energy loss is measured very precisely and a large amount of data is available for them, hence in a 0.1 GeV/c wide momentum interval the pion distribution is actually the sum of many Gaussians with different means and widths for different momentum ranges. For the kaons and protons less data are available so that a single Gaussian is sufficient to describe their peaks. Furthermore, from the fit can be seen that the electron Gaussian lies not exactly at 0 and has a width $\sigma \neq 1$, which indicates a not optimal parametrization of the $n\sigma_e^{\mathrm{TPC}}$ distribution. Figure 3.19 also shows that not all values of the pull distribution are spread between –2 and 2, indicating that the fit is not perfect. This could come from the imperfect model for the signal and background description. The fits can still provide decent values for the purity and the efficiency, since they are stable enough to extract the values and no structure is recognizable in the pull distribution, meaning that the fit function follows the trend of the data. As it can be seen, for p between 0.4 and 0.5 GeV/c, the kaon band is very close to the electron band, with a separation power of only 2σ. Still, the kaons can be fitted separately from the electrons. In the next momentum range, $0.5 < p < 0.6$ GeV/c, the two bands fully overlap. This is taken into account when determining the purity of the sample. For that, the kaon to electron ratio of the previous range ($\approx 7.8 \cdot 10^{-2}$) is subtracted from the purity estimated by the fit. For $0.6 < p < 0.7$ GeV/c the kaon band is between the electron and the pion bands and can be fitted separately again, while for higher momenta it merges with the pion band. In this momentum interval, also the proton peak can be seen. However, it is more than 10σ separated from the electrons, hence can be neglected in this fit. The protons come closer to the electron band for higher momenta, showing the same behavior as the kaons: they can be fitted separately up to $p = 1$ GeV/c, where however the separation power is only $\approx 0.6\sigma$, hence the purity is very low ($\approx 82\%$). Then, in the momentum range $1.0 < p < 1.1$ GeV/c, the proton and the electron bands fully overlap. Therefore, the same method is applied again: the proton to electron ratio of the previous momentum interval ($\approx 2.3 \cdot 10^{-1}$) is used to correct the purity. In the next momentum range, $1.1 < p < 1.2$ GeV/c, the proton peak lies on the other side of the electrons and can be fitted separately again, while for even higher momenta it merges with the pions. The fitted $n\sigma_e^{\mathrm{TPC}}$ distributions for $0.9 < p < 1.0$, $1.0 < p < 1.1$ and $1.1 < p < 1.2$ GeV/c are shown in figure 3.20 for no pion rejection as well as for the $4\sigma_\pi$ cut.

The purity and the efficiency as a function of momentum are discussed in the next chapter.

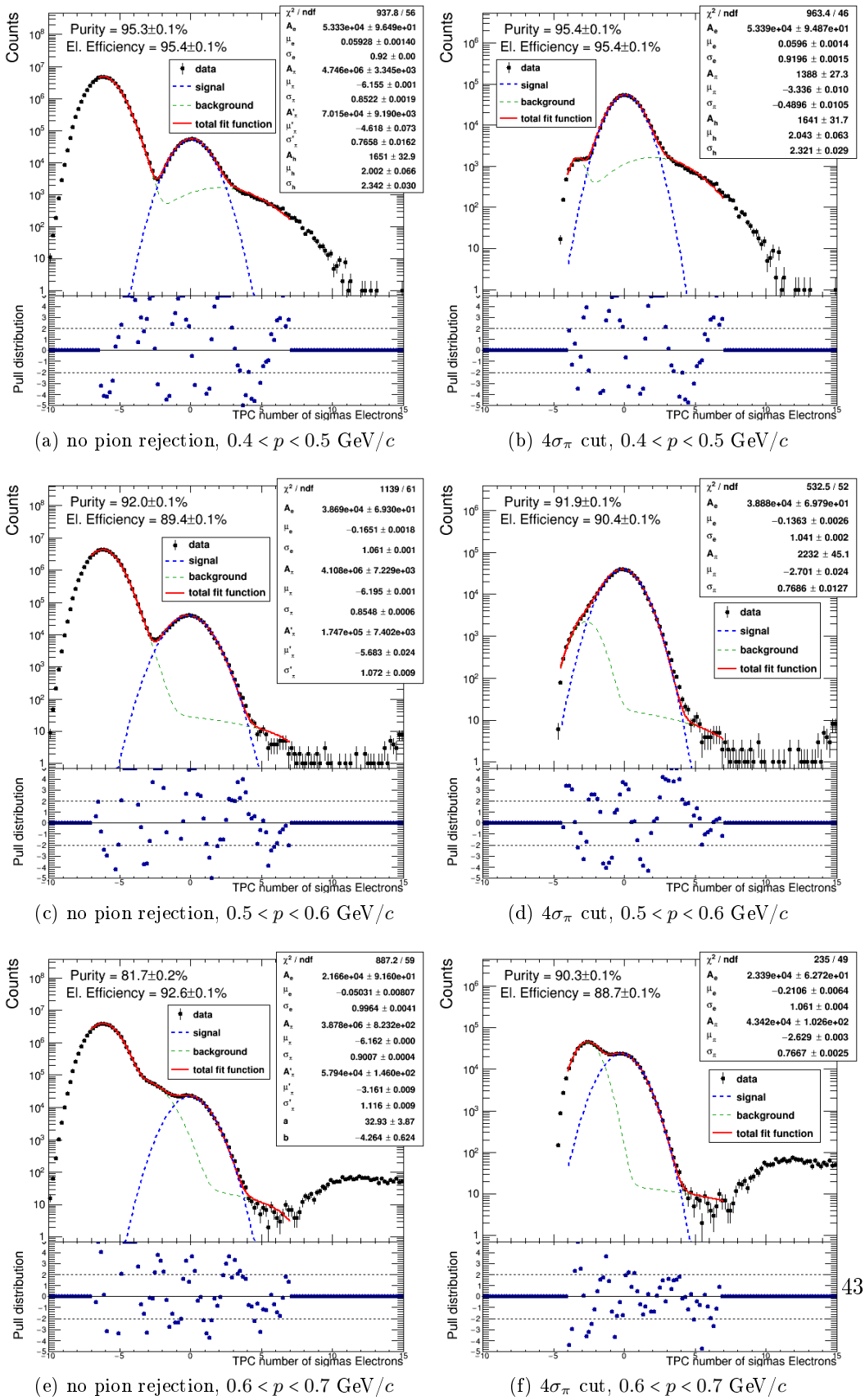

(a) no pion rejection, $0.4 < p < 0.5$ GeV/c

(b) $4\sigma_\pi$ cut, $0.4 < p < 0.5$ GeV/c

(c) no pion rejection, $0.5 < p < 0.6$ GeV/c

(d) $4\sigma_\pi$ cut, $0.5 < p < 0.6$ GeV/c

(e) no pion rejection, $0.6 < p < 0.7$ GeV/c

(f) $4\sigma_\pi$ cut, $0.6 < p < 0.7$ GeV/c

Figure 3.19: $n\sigma_e^{\mathrm{TPC}}$ distribution without pion rejection (left) and $4\sigma_\pi$ cut (right) in the momentum range $0.4 < p < 0.7$ GeV/c. It can clearly be seen how the kaons cross the electron band in this momentum range.

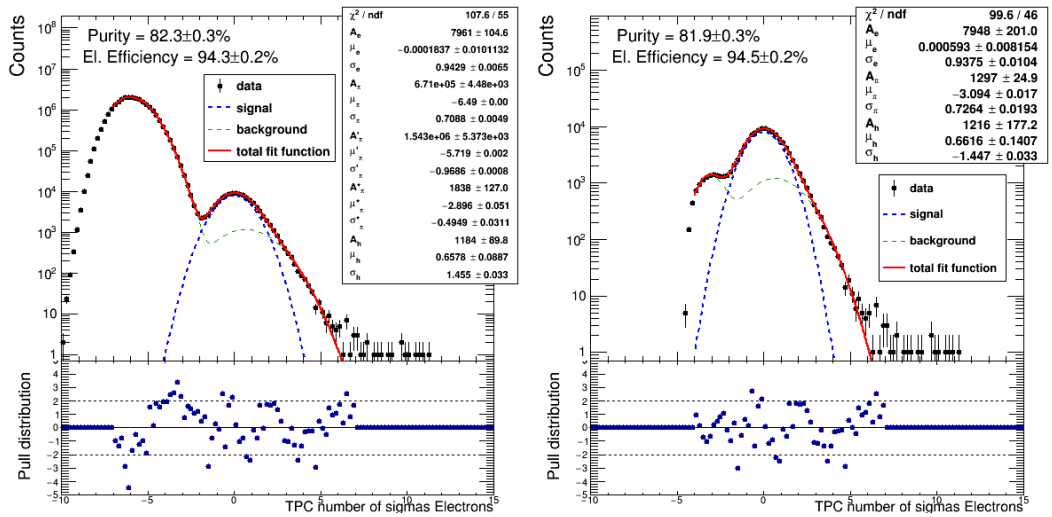

(a) no pion rejection, $0.9 < p < 1.0$ GeV/c

(b) $4\sigma_\pi$ cut, $0.9 < p < 1.0$ GeV/c

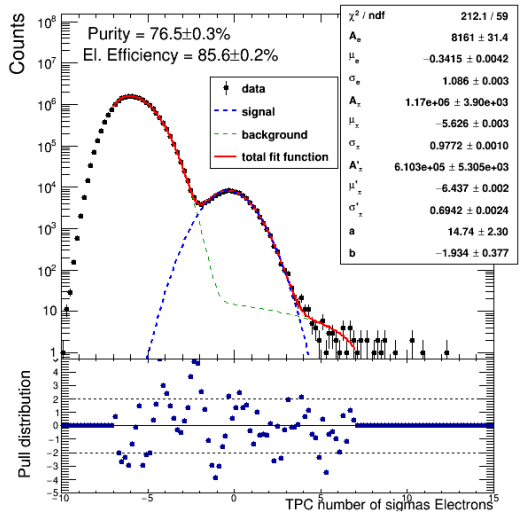

(c) no pion rejection, $1.0 < p < 1.1$ GeV/c

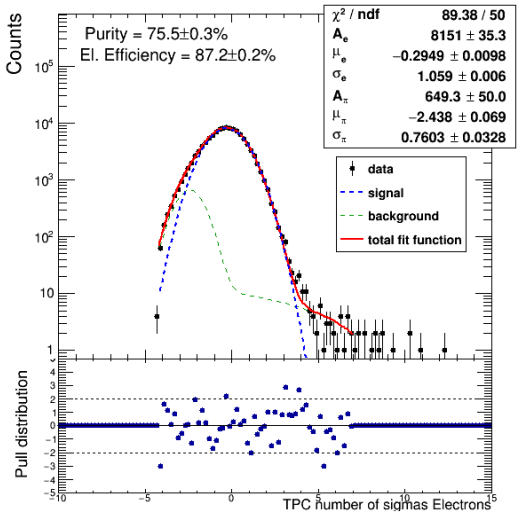

(d) $4\sigma_\pi$ cut, $1.0 < p < 1.1$ GeV/c

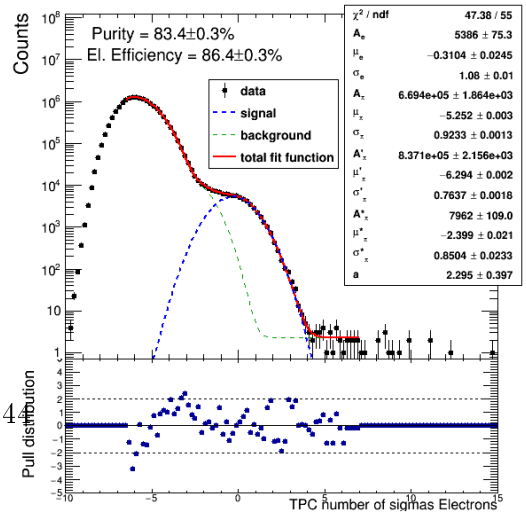

(e) no pion rejection, $1.1 < p < 1.2$ GeV/c

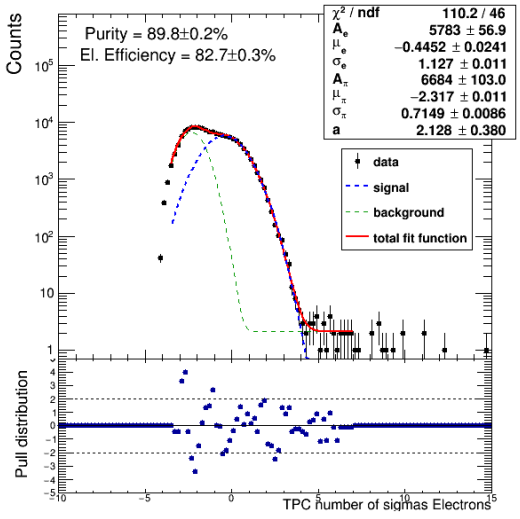

(f) $4\sigma_\pi$ cut, $1.1 < p < 1.2$ GeV/c

Figure 3.20: $n\sigma_e^{\mathrm{TPC}}$ distribution without pion rejection (left) and $4\sigma_\pi$ cut (right) in the momentum range $0.9 < p < 1.2$ GeV/c. It can clearly be seen how the protons cross the electron band in this momentum range.

Chapter 4

Results

In this chapter, the purity and the efficiency of single electrons are discussed as a function of momentum for the ITS/TPC/TOFif selection. Then, from the single electron result the purity of dielectrons is determined as a function of invariant mass, and finally, the purity of the signal is extracted.

4.1 Single Electron Purity and Efficiency

From the fits of the $n\sigma_{\pi}^{\mathrm{TPC}}$ vs. $n\sigma_{e}^{\mathrm{TPC}}$ distribution discussed in the last section of the analysis chapter, the purity and the efficiency of the ITS/TPC/TOFif PID set has been extracted as a function of momentum.

The purity vs. p distribution can be seen in figure 4.1 both without pion rejection and $4\sigma_{\pi}$ cut. The statistical uncertainties on the purity are smaller than the marker size. As shown in the figure, for the lowest momentum range, $0.2 < p < 0.3$ GeV/c, the purity of the cut without pion rejection amounts to $\approx 90\%$, while the $4\sigma_{\pi}$ cut increases it significantly: the purity becomes $\approx 100\%$, since the pion rejection removes all pions, and the kaons and protons are still more than 15σ separated from the electrons, hence they do not contaminate the electron sample. In the next momentum interval, 0.3 to 0.4 GeV/c, the purity is still $\approx 100\%$ both for no pion rejection as for the $4\sigma_{\pi}$ cut, denoting a very good separation between pions, electrons and kaons in this p range. Then, a continuous drop of the purity is observed in the next three momentum ranges, due to the kaon band which gets closer to the electron band overlapping with it for $0.6 < p < 0.7$ GeV/c. In this interval, the pion rejection increases the purity from a value of $\approx 82\%$ to $\approx 90\%$. For p between 0.7 and 0.8 GeV/c the kaons merge already with the pions while the protons are still more than 10σ separated from the electrons, hence the purity increases again, reaching a value of 95% without pion rejection and of 97% with $4\sigma_{\pi}$ rejection. After that, the crossing of the protons through the electron band is easily recognizable in the purity trend from 0.8 to 1.4 GeV/c: the values of the purity get smaller with increasing momentum until they reach a minimum of $\approx 76\%$ for $1.0 < p < 1.1$ GeV/c, where the protons and electrons overlap. Here, one can notice that the purity of the $4\sigma_{\pi}$ cut (75.5%) is lower than without pion rejection (76.5%). This is likely due to the fact that after the $4\sigma_{\pi}$ cut only few candidates are

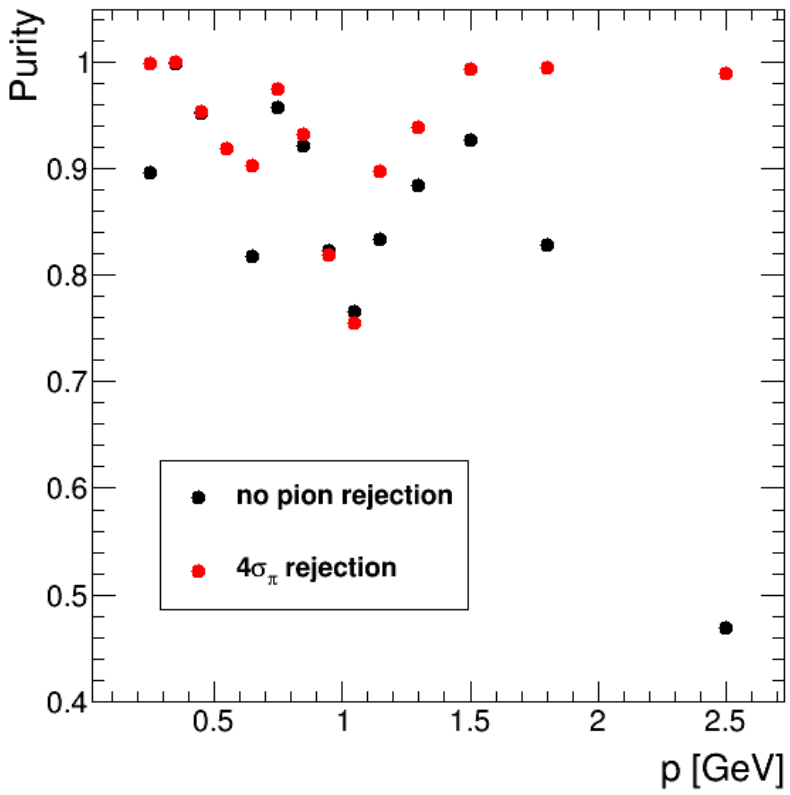

Figure 4.1: Purity of the ITS/TPC/TOFif selection as a function of momentum in p+p collisions at $\sqrt{s} = 7$ TeV.

left to fit the pion peak and hence the background cannot be described very precisely. This relative difference of 1.3% also means that the absolute systematic uncertainties of the fits have to be at least 1.3%. For higher momenta ($p > 1.1$ GeV/c) and no pion rejection, the purity first increases as the proton band merges with the pion band, reaching a value of $\approx 92\%$ for $1.4 < p < 1.6$ GeV/c, and then drops again, getting very low ($\approx 47\%$) for $p > 2$ GeV/c. This is due to the momentum dependence of the separation power between pions and electrons. The $4\sigma_\pi$ cut instead leads for $p > 1.1$ GeV/c to higher purity values in each momentum interval, since the pion rejection removes not only pions but also kaons and protons. For momenta higher than 1.4 GeV/c, the purity reaches very high values of $\approx 99\%$.

To summarize, the $4\sigma_\pi$ cut always provides higher purity values compared to no rejection, with exception of the momentum interval from 0.9 to 1.1 GeV/c, where, however, the difference is only 1.3%. Hence, one can safely say that the pion rejection significantly improves the electron identification in the TPC.

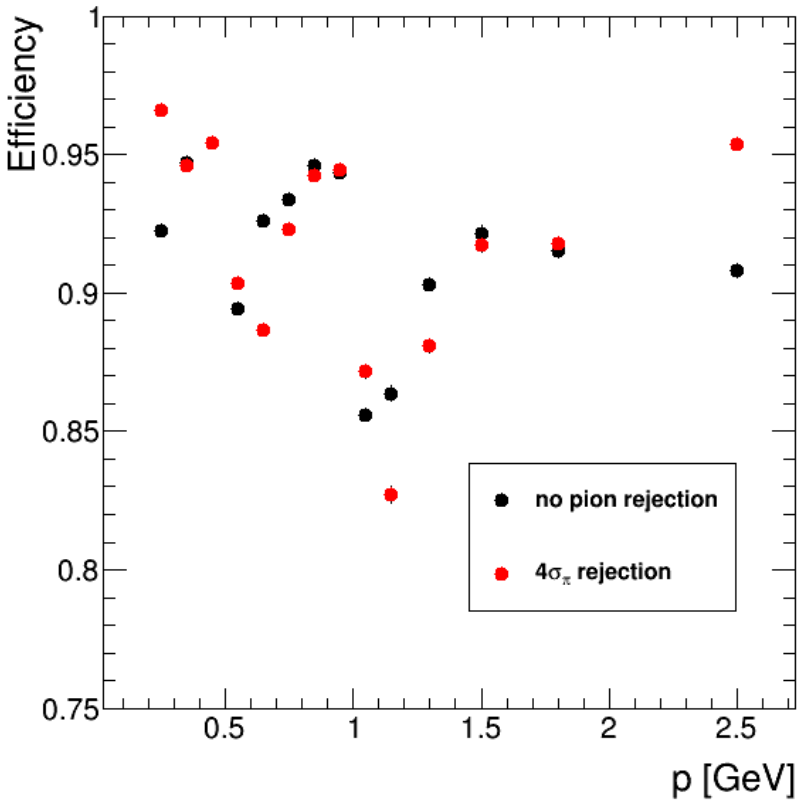

Figure 4.2: Relative efficiency of the ITS/TPC/TOFif selection as a function of momentum in p+p collisions at $\sqrt{s} = 7$ TeV.

In figure 4.2, the relative efficiency of the ITS/TPC/TOFif cut is shown as a function of momentum both without pion rejection and with a $4\sigma_\pi$ cut, with again statistical uncertainties smaller than the marker size. Since for the determination of the efficiency only the electron fit function is considered, the efficiency is expected to be approximately constant. However, as can be seen in figure 4.2, it fluctuates between $\approx 85\%$ and $\approx 95\%$ without pion rejection and $\approx 82\%$ and $\approx 97\%$ with a $4\sigma_\pi$ cut. This is mainly due to the non-optimal parametrization of the $n\sigma_e^{\mathrm{TPC}}$ distribution at the calibration step of the ALICE data reconstruction, since this leads to different means and widths of the Gaussians fitted to the electron peak for different momenta, hence to different efficiency values. Figure 4.2 also shows that in some momentum ranges the relative efficiency of the $4\sigma_\pi$ cut is higher than without rejection. This comes from the signal loss due to the cut on $n\sigma_\pi^{\mathrm{TPC}}$: this removes also a small fraction of electrons, which however affects only the integral of the electron fit function in the whole $n\sigma_e^{\mathrm{TPC}}$ range (the denominator in formula 3.17), and not the integral in the

range $-1.5 < n\sigma_e^{\mathrm{TPC}} < 3$. Hence, with the denominator getting smaller, the efficiency seemingly gets higher.

Since the ITS/TPC/TOFif cut has the second highest statistical significance with a purity much higher than the TPC-only cut, it proves to be the most appropriate to identify electrons among the PID sets analyzed in this thesis. Hence for this set, first the purity of the dielectron pairs is determined from the single electron result and then the signal purity is calculated in the next sections.

4.2 Dielectron Purity

For the dielectron purity, the three dielectron distributions obtained from the combination of each electron with all other electrons coming from the same event, i.e. N_{+-}, N_{++} and N_{--}, are considered again. The purity of a dielectron pair is given by the product of the two single electrons purities, which are assigned to the electrons composing the pair depending on their momentum:

$$P_{ee}\left(m_{ee}\right) = P_{e_1}\left(p_1\right) \cdot P_{e_2}\left(p_2\right) \tag{4.1}$$

From the momentum vectors of the single electrons, the invariant mass of the pair can be determined according to equation 3.2. Hence, the pair purity can be studied as a function of invariant mass. However, since an invariant mass value can be obtained through different combinations of momenta, for each of these values one gets a purity distribution instead of one fixed value, therefore the mean purity is considered. Figure 4.3 shows the mean pair purity as a function of invariant mass for all three charge combinations: $P_{N_{+-}}$, $P_{N_{++}}$ and $P_{N_{--}}$. As it can be seen, the three distributions have a very similar trend with a mean purity always higher than 85%. The highest values are reached for $m_{ee} < 0.7$ GeV/c^2, where it amounts to 90–95%. Then, the purity drops down to $\approx$ 85% in the intermediate mass region and increases again for high invariant mass values, although with bigger fluctuations for m_{ee} higher than ≈ 3 GeV/c^2, which are due to the large statistical uncertainties of the data. The trend of the purity distributions reflects the purity of the average momentum of the single electrons composing a pair with a certain invariant mass: small invariant mass values are most probably obtained by the combination of two low-momentum electrons, which have a very high purity. In the intermediate mass region, the average single electron momentum is higher and has a higher probability to fall into the ranges where kaons and protons cross the electron band, i.e. where the purity is lower. Therefore, also the mean dielectron purity is lower. For even higher invariant masses, the average momentum of the single electrons is higher too, which corresponds to higher single purity values. Hence, the dielectron purity increases again.

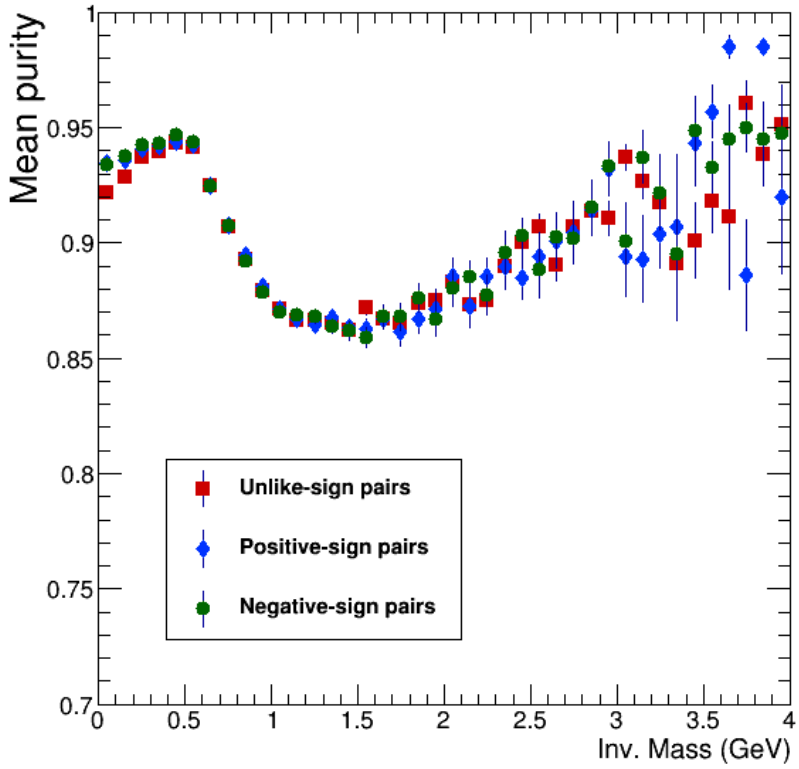

Figure 4.3: Mean dielectron purity as a function of invariant mass in p+p collisions at $\sqrt{s} = 7$ TeV.

4.2.1 Signal Purity

From the dielectron purity distributions $P_{N_{+-}}$, $P_{N_{++}}$ and $P_{N_{--}}$, the signal purity of the ITS/TPC/TOFif cut can be derived. It can be calculated from the purity of the unlike-sign pairs, $P_{N_{+-}}$, which is equal to the weighted sum of the signal and background purities, P_S and P_B, since $N_{+-} = S + B$:

$$P_{N_{+-}} = P_S \cdot \frac{S}{N_{+-}} + P_B \cdot \frac{B}{N_{+-}}. \tag{4.2}$$

From this equation, one obtains the purity of the signal:

$$\begin{aligned} P_S &= \left(P_{N_{+-}} \cdot N_{+-} - P_B \cdot B\right)/S \\ &= P_{N_{+-}} \cdot \left(\frac{B}{S} + 1\right) - P_B \cdot \frac{B}{S}, \end{aligned} \tag{4.3}$$

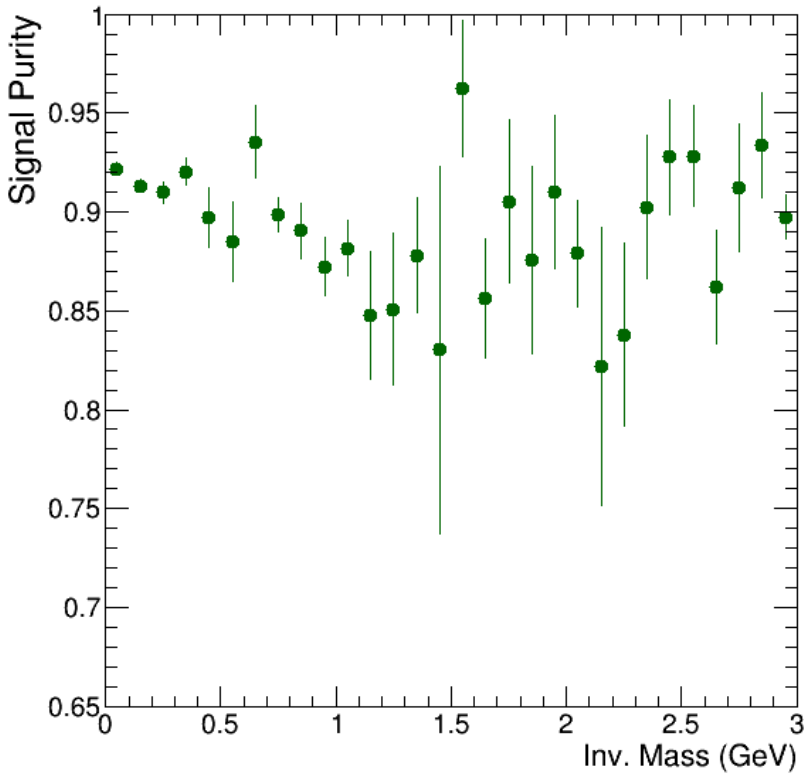

Figure 4.4: Signal purity of the ITS/TPC/TOFif PID set as a function of invariant mass in p+p collisions at $\sqrt{s} = 7$ TeV.

with P_B the weighted sum of the like-sign purities:

$$P_B = P_{N_{++}} \cdot \frac{N_{++}}{B} + P_{N_{--}} \cdot \frac{N_{--}}{B}. \tag{4.4}$$

The signal purity of the ITS/TPC/TOFif cut is shown in figure 4.4 as a function of invariant mass. As it can be seen, the signal shows a purity higher than $\approx 82\%$. For some invariant mass values, the purity presents large statistical errors, which are due to small S/B ratios. The signal purity distribution reflects the fact that the dielectron signal contains a variety of physics sources, therefore it varies more than the purity of the N_{+-} distribution, which is dominated by combinatorial background. However, a trend roughly similar to the unlike- and like-sign purities in figure 4.3 can be recognized: for low and high invariant mass values the signal purity is higher, while the lowest purity values appear in the intermediate mass region, a behavior that

originates again from the average single electron momentum changing with invariant mass.

Chapter 5

Summary and Outlook

In this thesis, four different PID sets were analyzed with the aim of optimizing the identification of electrons produced in pp collisions at $\sqrt{s} = 7$ TeV. The criteria used to decide which of them is the most appropriate to identify electrons were the statistical significance S/σ_S of the dielectron signal, studied as a function of invariant mass, and the single electron purity as a function of momentum. A combined electron selection in the $n\sigma_e$ vs. p distributions of the ITS, TPC and TOF detectors, showed the second highest statistical significance and a high single electron purity (75–100%), while the PID set with the highest S/σ_S ratio showed a very low purity, denoting a large hadron contamination of the signal. Therefore, the ITS/TPC/TOFif cut proved to be the most appropriate to identify electrons among the four analyzed in this thesis. For this set, the dielectron purity and the purity of the signal were determined as a function of invariant mass. The signal shows a purity higher than 82%.

In the future, one could optimize the model used to fit the data in order to extract the single electron purity, since the fits were not perfect although stable enough to determine the purity. For example, instead of parametrizations of signal and background shapes, templates could be used, which are a description of the energy loss distributions of the particles obtained via Monte Carlo simulations. A study of the systematic uncertainties of the fits should be performed too. Furthermore, an ITS/TPC/TOF cut which always uses the TOF signal, instead of requiring it only if the particle hit the detector, could be analyzed in order to check if it leads to a higher purity without losing in statistical significance. Finally, a fine tuning of the PID sets could be done, i.e. the limits of the electron inclusion in each $n\sigma_e$ vs. p distribution as well as of the pion rejection in the TPC could be changed, in order to see if this leads to a higher statistical significance, although an approximate estimation of this was done before performing the analysis presented in this thesis, and showed that the variation of the significance is mostly negligible.

The main result of this thesis, the signal purity of the ITS/TPC/TOFif PID set, will be used in the dielectron analysis of the LHC 2010 pp data which will be published soon. Furthermore, the framework developed for the data analysis of this thesis can be used to improve the electron identification in the analysis of the 2010

Pb-Pb collision data. This work can also be an input for the analysis of the 2015 pp data at $\sqrt{s} = 13$ TeV, where the gas filling the TPC detector has changed (Ar/CO_2 instead of Ne/CO_2), and hence the PID sets for the electron identification must be tuned again since the detector response is different.

Appendix A

Complete List of the TOF-based Approach

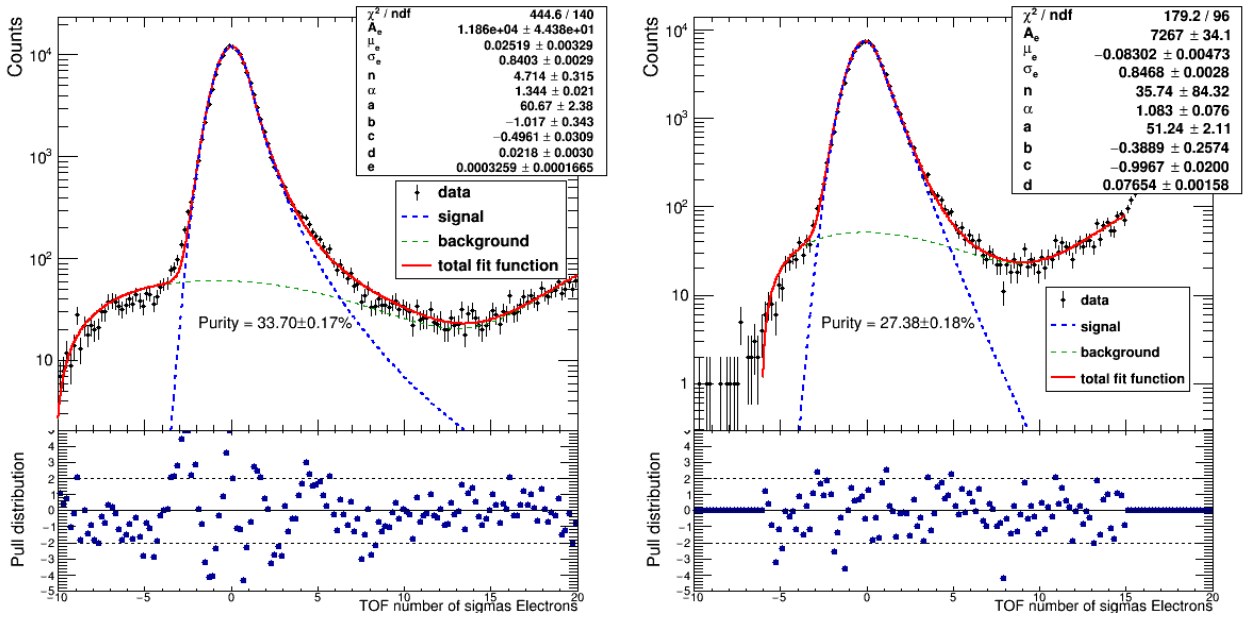

(a) $0.4 < p < 0.5$ GeV/c (b) $0.6 < p < 0.7$ GeV/c

Figure A.1: $n\sigma_e^{\mathrm{TOF}}$ distributions in the momentum ranges 0.4–0.5 and 0.6–0.7 GeV/c. From the fits the purity of the TPC-only cut is extracted.

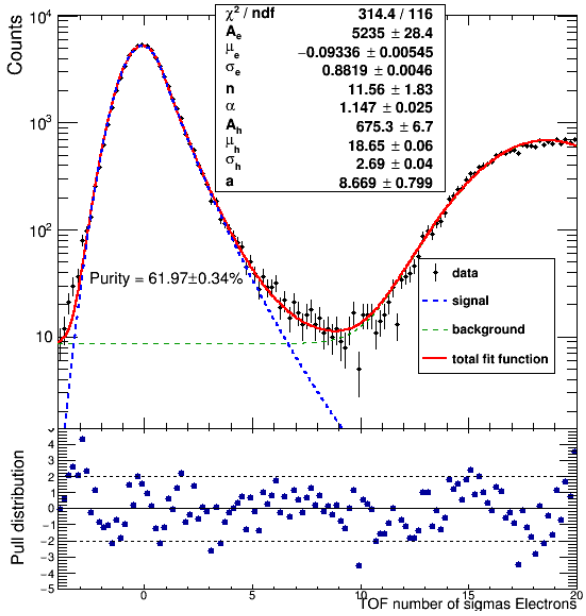

(a) $0.7 < p < 0.8$ GeV/c

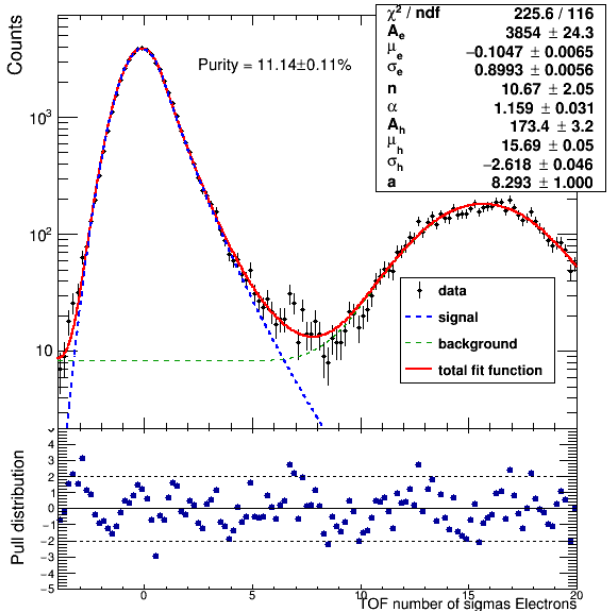

(b) $0.8 < p < 0.9$ GeV/c

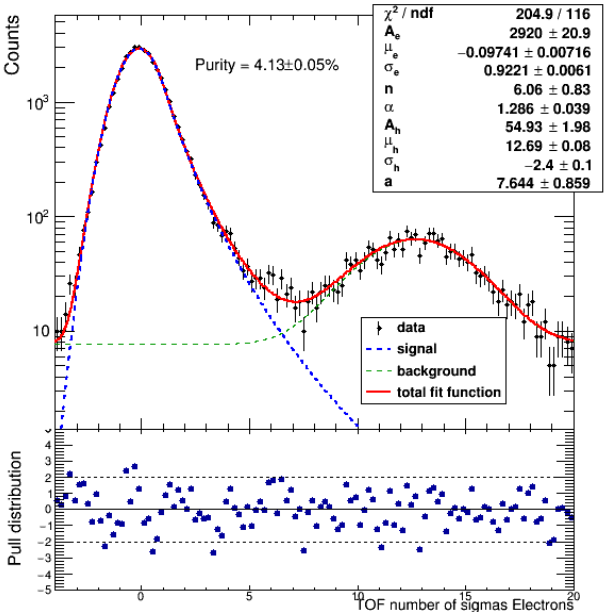

(c) $0.9 < p < 1.0$ GeV/c

Figure A.2: $n\sigma_e^{\mathrm{TOF}}$ distributions in the momentum ranges $0.7 < p < 1.0$ GeV/c. From the fits the purity of the TPC-only cut is extracted.

Appendix B

Complete List of the TPC-based Approach

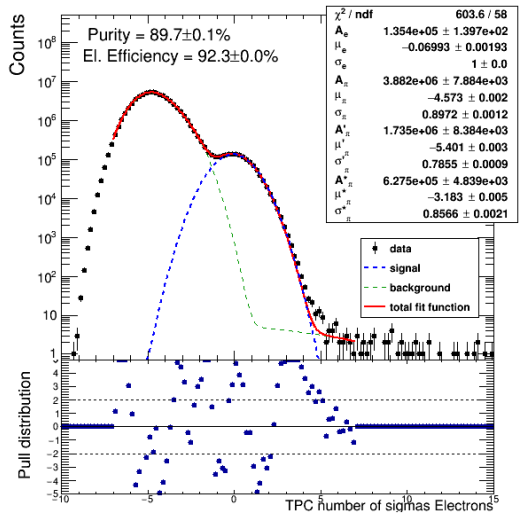

(a) no pion rejection, $0.2 < p < 0.3$ GeV/c

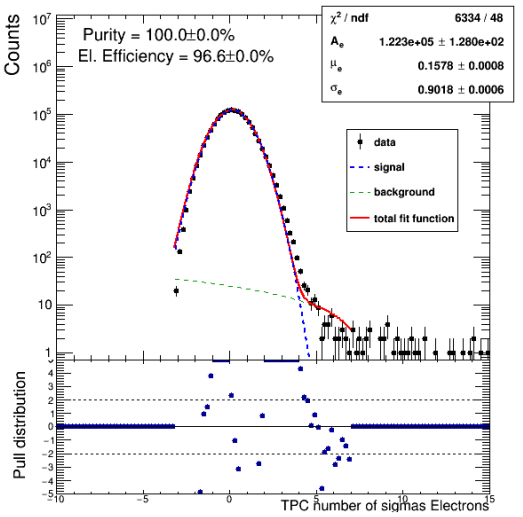

(b) $4\sigma_\pi$ cut, $0.2 < p < 0.3$ GeV/c

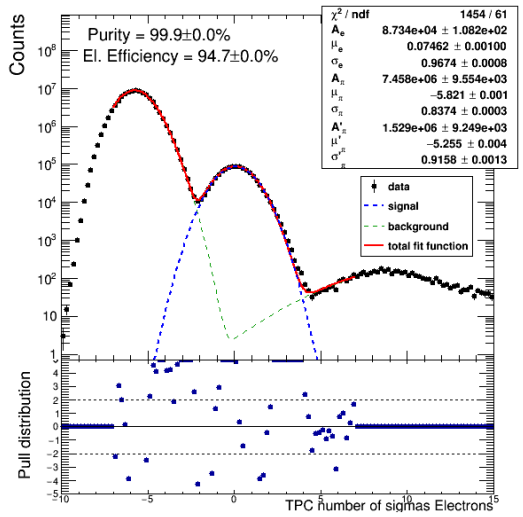

(c) no pion rejection, $0.3 < p < 0.4$ GeV/c

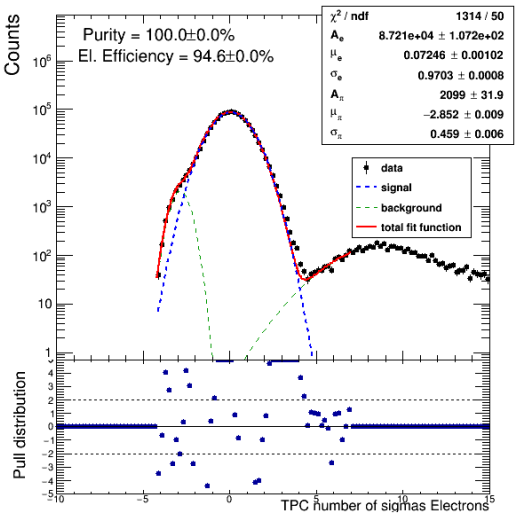

(d) $4\sigma_\pi$ cut, $0.3 < p < 0.4$ GeV/c

Figure B.1: $n\sigma_e^{\mathrm{TPC}}$ distribution without pion rejection (left) and with a $4\sigma_\pi$ cut (right) in the momentum ranges $0.2 < p < 0.4$ GeV/c. From the fits the purity and the relative efficiency of the ITS/TPC/TOFif cut are extracted.

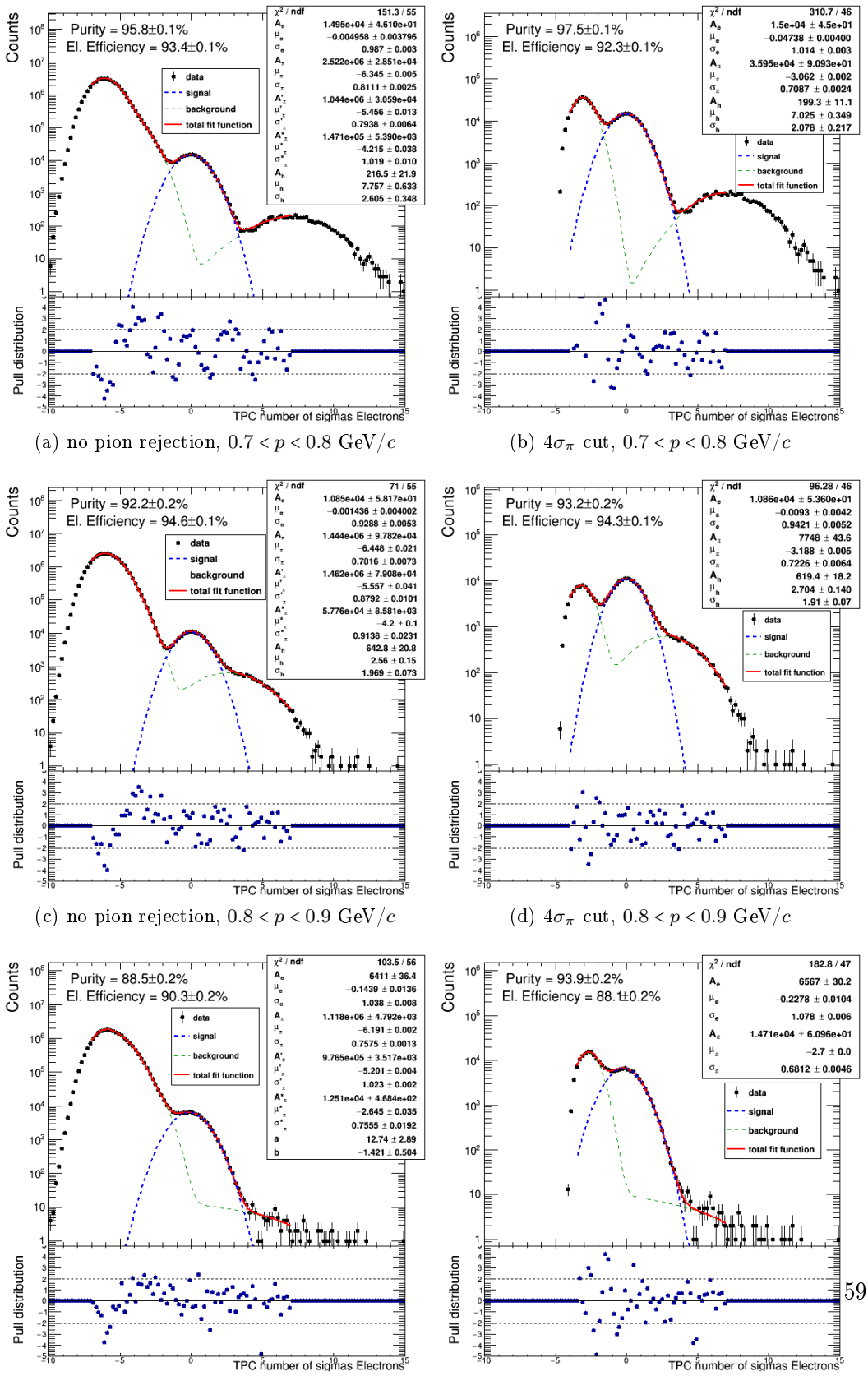

(a) no pion rejection, $0.7 < p < 0.8$ GeV/c

(b) $4\sigma_\pi$ cut, $0.7 < p < 0.8$ GeV/c

(c) no pion rejection, $0.8 < p < 0.9$ GeV/c

(d) $4\sigma_\pi$ cut, $0.8 < p < 0.9$ GeV/c

(e) no pion rejection, $1.2 < p < 1.4$ GeV/c

(f) $4\sigma_\pi$ cut, $1.2 < p < 1.4$ GeV/c

Figure B.2: $n\sigma_e^{\mathrm{TPC}}$ distribution without pion rejection (left) and with a $4\sigma_\pi$ cut (right) in the momentum ranges $0.7 < p < 0.9$ and $1.2 < p < 1.4$ GeV/c. From the fits the purity and the relative efficiency of the ITS/TPC/TOFif cut are extracted.

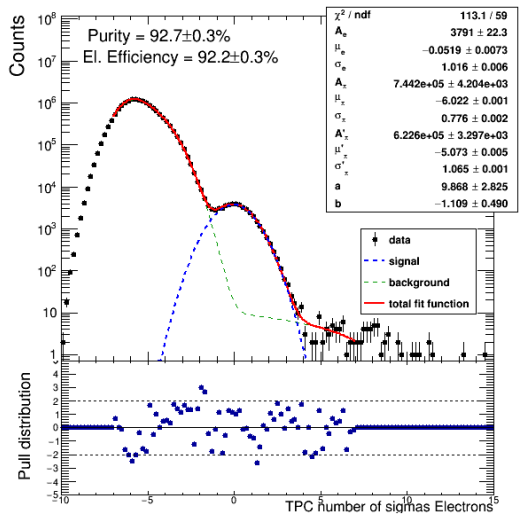

(a) no pion rejection, $1.4 < p < 1.6$ GeV/c

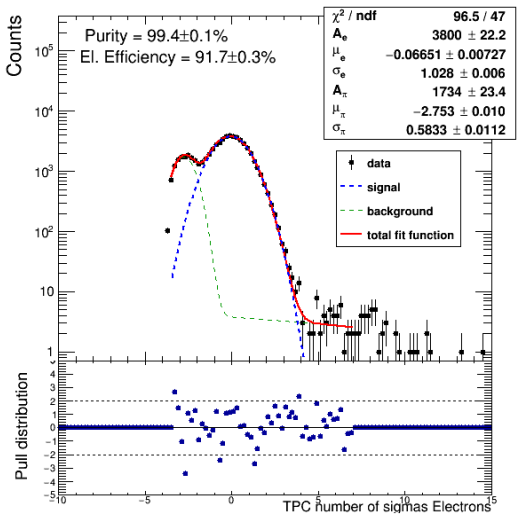

(b) $4\sigma_\pi$ cut, $1.4 < p < 1.6$ GeV/c

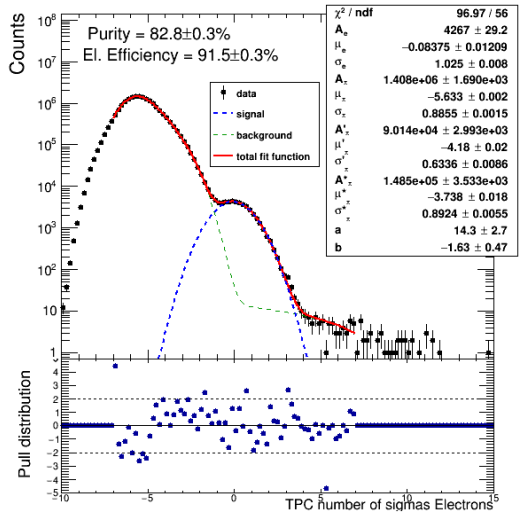

(c) no pion rejection, $1.6 < p < 2.0$ GeV/c

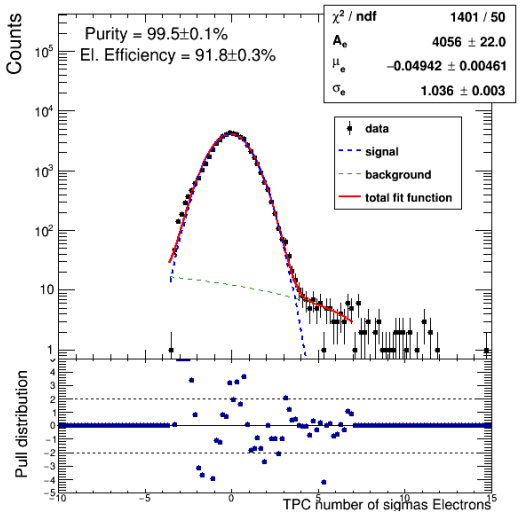

(d) $4\sigma_\pi$ cut, $1.6 < p < 2.0$ GeV/c

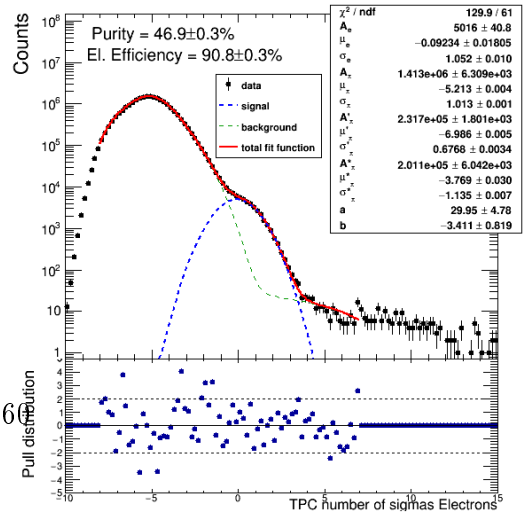

(e) no pion rejection, $2.0 < p < 8.0$ GeV/c

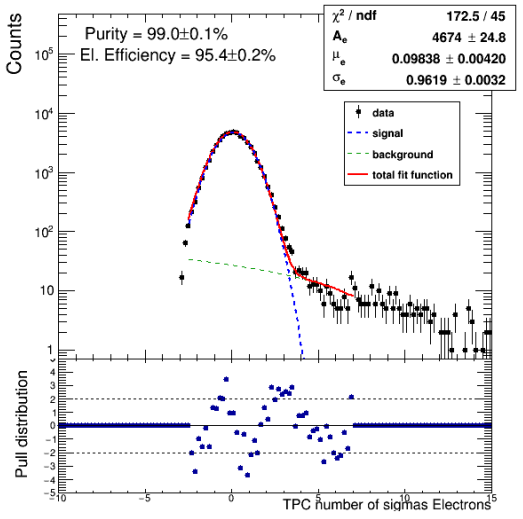

(f) $4\sigma_\pi$ cut, $2.0 < p < 8.0$ GeV/c

Figure B.3: $n\sigma_e^{\mathrm{TPC}}$ distribution without pion rejection (left) and with a $4\sigma_\pi$ cut (right) in the momentum ranges $1.4 < p < 8.0$ GeV/c. From the fits the purity and the relative efficiency of the ITS/TPC/TOFif cut are extracted.

Bibliography

[1] Edward V. Shuryak. »Quark-Gluon Plasma and Hadronic Production of Leptons, Photons and Psions«. In: *Phys. Lett.* B78 (1978). [Yad. Fiz.28,796(1978)], p. 150. DOI: 10.1016/0370-2693(78)90370-2.

[2] Szabolcs Borsanyi et al. »Is there still any T c mystery in lattice QCD? Results with physical masses in the continuum limit III«. In: *Journal of High Energy Physics* 2010.9 (2010), pp. 1–26.

[3] G. Agakichiev et al. »e+ e- pair production in Pb - Au collisions at 158-GeV per nucleon«. In: *Eur. Phys. J.* C41 (2005), pp. 475–513. DOI: 10.1140/epjc/s2005-02272-3. arXiv: nucl-ex/0506002 [nucl-ex].

[4] R. Arnaldi et al. »First measurement of the rho spectral function in high-energy nuclear collisions«. In: *Phys. Rev. Lett.* 96 (2006), p. 162302. DOI: 10.1103/PhysRevLett.96.162302. arXiv: nucl-ex/0605007 [nucl-ex].

[5] S. Afanasiev et al. »Enhancement of the dielectron continuum in s(NN)**(1/2) = 200-geV Au+Au collisions«. In: (2007). arXiv: 0706.3034 [nucl-ex].

[6] A. Adare et al. »Dielectron production in Au+Au collisions at $\sqrt{s_{NN}}$=200 GeV«. In: (2015). arXiv: 1509.04667 [nucl-ex].

[7] L. Adamczyk et al. »Dielectron Mass Spectra from Au+Au Collisions at $\sqrt{s_{\mathrm{NN}}}$ = 200 GeV«. In: *Phys. Rev. Lett.* 113.2 (2014). [Addendum: Phys. Rev. Lett.113,no.4,049903(2014)], p. 022301. DOI: 10.1103/PhysRevLett.113.022301,10.1103/PhysRevLett.113.049903. arXiv: 1312.7397 [hep-ex].

[8] L. Adamczyk et al. »Energy dependence of acceptance-corrected dielectron excess mass spectrum at mid-rapidity in Au+Au collisions at $\sqrt{s_{NN}}$ = 19.6 and 200 GeV«. In: *Phys. Lett.* B750 (2015), pp. 64–71. DOI: 10.1016/j.physletb.2015.08.044. arXiv: 1501.05341 [hep-ex].

[9] *ALICE figure repository*. 2012. URL: https://aliceinfo.cern.ch/Figure/performance_fig.

[10] ALICE collaboration et al. »Performance of the ALICE Experiment at the CERN LHC«. In: *International Journal of Modern Physics A* (2014).

[11] ALICE Collaboration, K Aamodt et al. »The ALICE experiment at the CERN LHC«. In: *Jinst* 3.420 (2008), S08002.

[12] Johan Alme et al. »The ALICE TPC, a large 3-dimensional tracking device with fast readout for ultra-high multiplicity events«. In: *Nuclear Instruments and Methods in Physics Research Section A: Accelerators, Spectrometers, Detectors and Associated Equipment* 622.1 (2010), pp. 316–367.

[13] K. A. Olive et al. »Review of Particle Physics«. In: *Chin. Phys.* C38 (2014), p. 090001. DOI: 10.1088/1674-1137/38/9/090001.

[14] Martin Völkl. »Study of the Transverse Momentum Spectra of Semielectronic Heavy Flavour Decays in pp-Collisions at $\sqrt{s} = 7$ TeV«. Masterthesis. University of Heidelberg, 2012.

[15] A Akindinov et al. »The commissioning of the ALICE time-of-flight detector and results from the 2008 cosmic-ray data taking«. In: *Nuclear Instruments and Methods in Physics Research Section A: Accelerators, Spectrometers, Detectors and Associated Equipment* 615.1 (2010), pp. 37–41.

[16] Christian Lippmann. »Particle identification«. In: *Nuclear Instruments and Methods in Physics Research Section A: Accelerators, Spectrometers, Detectors and Associated Equipment* 666 (2012), pp. 148–172.

[17] ALICE collaboration et al. »Performance of the ALICE VZERO system«. In: *Journal of Instrumentation* 8.10 (2013), P10016.

[18] B Alessandro et al. »ALICE: Physics performance report, volume II«. In: *Journal of Physics G: Nuclear and Particle Physics* 32.10 (2006), p. 1295.

Acknowledgements

The most special thanks and my sincere appreciation go to my supervisor Torsten Dahms for the time and effort he invested in my work over the last months. He introduced me to the complicated but fascinating world of particle physics with accelerators, taught me C++ programming and gave me the opportunity to participate in important conferences already as a bachelor student. For all this, I am very grateful to him. I also want to thank him for always taking time to answer my questions and for his encouragement and incomparable patience.

I am most thankful to Prof. Laura Fabbietti for giving me the opportunity to be part of her amazing working group and to write my thesis in the context of a particle physics experiment connected to the LHC.

Furthermore, I want to thank Ivan Vorobyev for explaining the dielectron analysis framework to me and providing me with the necessary data to perform my analysis. I also want to thank him and Oton for proofreading my thesis. Special thanks also go to Alex for providing me with inspirational music and to Barbara and my sister for their moral support.

Last, I would like to thank my parents for making it possible for me to study at the Technical University Munich and for supporting me in my courses of study.